ABSTRACT

Title of dissertation: Electron Distribution and Electrostatic Oscillations of an Ultracold Plasma

Kevin Allen Twedt,
Doctor of Philosophy, 2012

Dissertation directed by: Professor Steven Rolston
Department of Physics

Ultracold neutral plasmas (UCPs) are transient laboratory plasmas with many unique properties owing to their creation from the near-threshold photoionization of laser-cooled neutral atoms in an ultra-high vacuum environment. UCPs have equilibrium electron and ion temperatures as low as 1 K, orders of magnitude colder than other neutral plasmas. They are untrapped and expand into vacuum with an inhomogeneous density and changing neutrality. The plasmas are also created in a non-equilibrium state and the establishment of equilibrium results in a neutral plasma on the border of strong coupling. All of these features have made UCPs ideal systems for the study of basic plasma phenomena.

This thesis focuses on the long-time expansion of UCPs created from laser-cooled xenon atoms. We investigate the importance of external electric fields and the changing plasma neutrality which have been largely ignored in previous work. We present a detailed analysis of the electron distribution and the rate of electron loss during expansion. We show the effect of electron loss on plasma oscillations, and have developed a new technique to directly observe electrostatic plasma oscillations by measuring the induced current on a nearby electrode. We also expand on previous measurements of plasma expansion in a uniform magnetic field and consider the prospects for magnetic trapping.

ELECTRON DISTRIBUTION AND ELECTROSTATIC OSCILLATIONS OF AN ULTRACOLD PLASMA

by

Kevin Allen Twedt

Dissertation submitted to the Faculty of the Graduate School of the
University of Maryland, College Park in partial fulfillment
of the requirements for the degree of
Doctor of Philosophy
2012

Advisory Committee:
Professor Steven Rolston, Chair/Advisor
Professor Thomas Antonsen
Professor Ki-Yong Kim
Professor Patrick O'Shea
Dr. James Porto

Acknowledgments

The work in this thesis was made possible by many individuals, the first of which is my adviser Steve Rolston. I thank Steve for his guidance over the past several years, and his willingness to let me, an inexperienced graduate student, pursue my own research directions in the lab. The initial stages of my research were done in collaboration with Xianli Zhang, and I am very grateful to him for his patience in teaching me the basics of our experimental apparatus and getting me on my feet as an experimental physicist. I have benefited from the work of the large number of former students and post-docs that have been through the xenon lab in the past 15 years. Their quality work has made my job easier. I must also thank them for leaving a few mysteries unsolved such that I always had plenty of work to do. I am glad to have had the help of Robert Perrotta, a UMD undergraduate student, for the past three years. Robert has made significant contributions to the work presented in this thesis, despite the varied projects and the vague and continuously changing goals that I set for him.

I have benefited greatly from conversations with all of my colleagues in the AMO group at Maryland, including Luis Orozco and Trey Porto and the students that have been in the group during my time here. I am thankful for the patience of all those in the Rolston group during the times when I turned our group meeting into a plasma physics discussion. I am indebted to all of my teachers and fellow students that have shaped my understanding of physics over the years, in particular my undergraduate advisers Cliff Chancey and Paul Shand and my good friends

David Norris, Ray Fermo and my wife Ellie.

The support I have received from my family and friends has been most important to me. I owe the biggest debt to my parents for their encouragement, and to my wife Ellie for her constant support.

Table of Contents

List of Figures

List of Abbreviations

UCP	Ultracold Plasma
DIH	Disorder-Induced Heating
TBR	Three-body Recombination
Xe*	Metastable xenon
MOT	Magneto-Optical Trap
MCP	Microchannel Plate
OCP	One-Component Plasma
MK	Michie-King

Chapter 1

The Xenon Ultracold Plasma

1.1 Introduction

Laser-cooling of neutral atoms is a well-established technique that allows for the trapping of small samples of neutral atomic gases at densities and temperatures on the order of 10^{10} cm^{-3} and 100 μK. Access to the extremely cold temperature regime has sparked a wide range of fascinating experiments in atomic, molecular and solid state physics. By photo-ionizing a sample of ultracold atoms near the ionization threshold, an ultracold neutral plasma (UCP) [1–3] can be formed with equilibrium temperatures orders of magnitude colder than conventional neutral plasmas, allowing for the study of basic plasma physics in the ultracold regime. Many conventional neutral plasmas have temperatures of at least 1 eV (10^4 K) because they are sustained by ionizing collisions between particles, but the creation of UCPs from cold atoms gives equilibrium ion and electron temperatures as low as 100 μeV (1 K). Compared to other transient laser-produced plasmas, UCPs are clean and simple systems, and the low temperature and density make the relevant time scales easy to access experimentally.

UCPs were first created in 1999 at NIST in Gaithersburg, MD using xenon atoms [4] in the same experimental apparatus used in this work. Since then, several other groups have produced UCPs from laser-cooled samples of rubidium [5, 6], cesium [5], strontium [7] and calcium [8], and also from NO molecules in a molecular beam [9]. Experiments on UCPs can generally be separated into two regimes: the initial equilibration of the system in the first μs after creation and the long-time hydrodynamic expansion of the plasma on the time-scale of a few hundred μs.

UCPs have drawn considerable interest due to the promise of a strongly coupled neutral plasma. Strongly coupled plasmas are predicted to exist in some astrophysical systems, but are notoriously difficult to create and study in the laboratory. A plasma is strongly coupled when the Coulomb interaction energy between the charged particles is greater than the thermal energy. This is characterized by the coupling parameter

$$\Gamma_{e,i} = \frac{e^2/(4\pi\epsilon_0 a)}{k_b T_{e,i}} \tag{1.1}$$

where $a = (4\pi n/3)^{-1/3}$ is the Wigner-Seitz radius, n is the plasma density, e is the electron charge, ϵ_0 is the electric constant, k_b is Boltzmann's constant and $T_{e,i}$ is the electron (ion) temperature. A coupling parameter $\Gamma > 1$ indicates strong coupling. Immediately after the atoms have been ionized, the ions in the resulting plasma have nearly the same kinetic energy as the neutral atoms ($T_{atoms} = 100$ μK) and the electron kinetic energy can be tuned by adjusting the frequency of the ionizing laser relative to the ionization threshold, with a practical lower limit of 0.1 - 1 K. These numbers would suggest that both components of the plasma are strongly coupled with $\Gamma_e \approx 10$ and $\Gamma_i \approx 1000$.

However, it was quickly realized that UCPs are created in an uncorrelated non-equilibrium state and the establishment of local thermal equilibrium destroys this strong coupling through disorder-induced heating (DIH) [10–12]. Both the electronic and ionic components undergo DIH, but the process is more important for the ions since they start out with such a low kinetic energy. Prior to ionization, the neutral atoms are randomly positioned with no spatial correlation within a Gaussian density distribution. After ionization, the potential energy associated with the strong Coulomb interactions between the ions gets converted into kinetic energy, raising the temperature of the ions from the neutral atom temperature to about 1 K and decreasing Γ_i to near unity.

The DIH in the ions happens in the first μs after plasma creation and multiple experiments have observed this phenomenon by directly measuring the velocity distribution of the ions with optical probes [13–15]. Despite the DIH, the ions remain near the boundary of strong coupling and recent experiments are probing the effect of this moderate coupling on plasma processes such as the ion collision rate and ion acoustic waves [16, 17].

The initial electron kinetic energy is set by the energy in the ionizing photon and can be set anywhere between 0.1 - 1000 K. DIH in the electrons happens on the time-scale of ns, but is only significant when the initial kinetic energy is set to values less than 10 K. The electrons then establish a global thermal equilibrium in the first μs at a temperature that leaves $\Gamma_e < 1$, even when the atoms are ionized as close to threshold as possible. A more important heating mechanism for the electrons is three-body recombination (TBR), where an electron and ion recombine to form a highly excited Rydberg atom, and a second electron provides momentum and energy conservation. The free electron carries away the binding energy as kinetic energy, increasing the average energy of plasma electrons. The TBR rate scales as $T_e^{-9/2}$ [18–20], and thus the heating is worse for colder initial temperatures. TBR begins during the initial equilibration and continues to be a major factor during the subsequent expansion of the plasma. Regardless of how low the initial electron energy is set, TBR acts to eventually increase T_e to 30-40 K, keeping the electrons solidly in the weakly coupled regime throughout the plasma lifetime with $\Gamma_e = 0.1 - 0.2$ [1, 21].

After initial equilibration, UCPs expand into the surrounding vacuum with lifetimes on the order of 100 μs. The initial density of the plasma is a Gaussian distribution inherited from the neutral atom cloud and the Gaussian distribution is mostly maintained during expansion. The expansion is driven by thermal electron pressure and is thus closely linked to the electron temperature, which is changing dynamically during expansion due to the competition between TBR heating and adiabatic and evaporative cooling. In many experiments, the initial electron energy is intentionally set to larger values, 50-1000 K, to avoid the complications of DIH and TBR and to allow for a simpler theoretical description of expansion. Because UCPs are open, freely expanding systems, electrons can evaporate out of the plasma, which also gives a time-dependence to the degree of neutrality of the system, further complicating the expansion dynamics.

Work in our lab has focused on studying the long-time expansion of the plasma. Previous work has measured the expansion rate of the plasma [22, 23], the electron temperature evolution [21, 24] and the rate of Rydberg atom formation [21, 25], confirming the influence of TBR in raising the electron temperature. There were also measurements of electron oscillations [21, 22], the identification of a high-frequency electron drift instability [26] and the reduced expansion of the plasma transverse to a uniform magnetic field [23]. This thesis builds on these previous experiments, with a focus on the influence of external electric fields and the changing plasma neutrality.

The thesis is organized as follows. Chapter 1 will describe the creation of an UCP in our lab from a cloud of laser-cooled xenon atoms. We give some background on the theory of plasma expansion, and discuss the available experimental probes. Chapter 2 will discuss the electron distribution of an UCP. We present calculations of the electron spatial distribution and how it is influenced by external electric fields that are an important part of our charged particle diagnostics. We use this calculation to explain the observed flux of electrons escaping the plasma.

In Chapter 3 we outline a new diagnostic for the detection of electron oscillations that has several advantages over previous methods. We measure plasma oscillations and investigate the importance of the electron spatial distribution in determining the resonant frequency. We also present the first observation of hybrid oscillations in a UCP. In chapter 4, we describe on-going work on the asymmetric expansion of UCPs in a uniform magnetic field. We finally discuss prospects for three-dimensional magnetic trapping of the plasma.

1.2 UCP Creation

The experimental apparatus is designed for the laser-cooling and trapping of metastable xenon (Xe*). Explanations of previous experiments performed can be

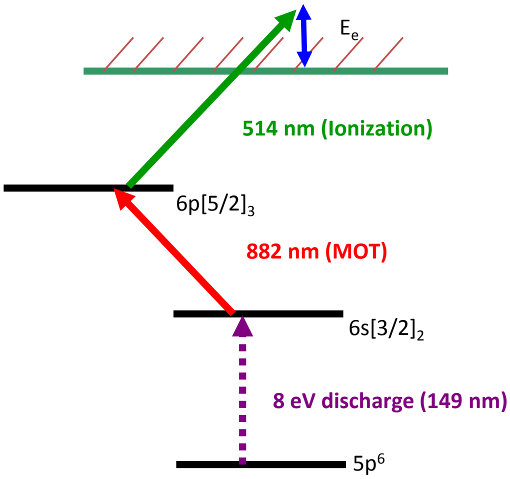

Figure 1.1: Xenon energy levels.

found in the theses of previous graduate students [27–30].

The details of the initial design of the apparatus are well explained in the thesis of Matt Walhout [27], which will be summarized here. Xenon gas enters the vacuum chamber through a quartz tube, with the flow of gas controlled by a variable leak valve. Inside the quartz tube is a tungsten rod held at -800 V. The end of the rod is a few mm away from a grounded skimmer aperture, and a dc glow discharge is struck between the two, the current limited by a ballast resistor to 2-3 mA. Through collisions with electrons inside the discharge, a small fraction ($10^{-4} - 10^{-5}$) of xenon atoms are excited to the metastable state $6s[3/2]_2$, 8 eV above the ground state. The metastable state has a 43 second lifetime [31], much longer than the experimental cycle, and serves as the ground state for laser-cooling. A level diagram of the relevant Xe* energy levels is shown in Fig. 1.1.

The xenon gas passes through the first skimmer, a differential pumping region and then an aperture before entering the Zeeman slower, where the metastable atoms are slowed as they approach the main science chamber. The apertures serve to collimate the beam of xenon atoms flowing into the slower.

The xenon gas contains all nine isotopes in their natural abundances. We can perform laser-cooling and trapping on any of the isotopes by adjusting the laser frequency. For this work, we exclusively work with ^{132}Xe as it is the most abundant and has no nuclear spin, and thus no hyperfine splitting of the laser-cooling transition, making a second frequency for optical pumping unnecessary.

Laser-cooling of neutral atoms is a well-established technique [32]. For Xe*, the $6s[3/2]_2$ - $6p[5/2]_3$ transition is a closed-cycling electric dipole transition at 882nm that we use for the laser cooling. A Titanium-Sapphire laser generates about 300 mW of 882 nm light. The Ti:Sa is locked to the laser-cooling transition using saturated absorption spectroscopy in a xenon reference cell. The reference cell is a glass tube filled with 700 mTorr neon gas and 7 mTorr xenon gas. To create Xe atoms in the metastable state, an rf inductively-coupled plasma discharge is created in the cell. The high percentage of Ne is required to sustain the plasma discharge, while having a small enough amount of Xe such that a probe laser is only partially absorbed, as required for the spectroscopy.

A portion of the locked laser light is detuned 130 MHz and sent down the length of the Zeeman slower, focused onto the second collimating aperture. The large detuning reflects the choice of the reversed field configuration for our Zeeman slower. The Ti:Sa also creates 5 beams for creation of the magneto-optical trap (MOT), and a probe beam used for imaging or ionization.

A schematic of the vacuum chamber is shown in Fig. 1.2. As Xe* atoms exit the Zeeman slower, they are collected and trapped in the MOT. The MOT consists of three orthogonal sets of counter-propagating laser beams and a pair of coils that produce a quadrupole magnetic field. The beams for two of the MOT axes are sent through wire mesh grids, needed for plasma diagnostics (Sec. 1.4), as shown in Fig. 1.2a. The grids allow 90% transmission, so four counter-propagating beams are used, instead of retro-reflecting two beams, to ensure proper power balance for the trap. The plane of these four beams is perpendicular to the axis of the MOT coils, and a fifth beam is directed along the coil axis and retro-reflected off a mirror as in Fig. 1.2b. The diffraction of the laser beams through the grids often imprints unique structure on the steady-state MOT density.

We typically load a few million atoms in the MOT in a loading time of 700 ms. The MOT has a roughly Gaussian density with a 300-500 μm radius and peak density of 10^{10} cm^{-3}. The steady-state number of atoms in the MOT is determined by the balance of trap loading and loss rates. The dominant loss mechanism for a Xe* MOT is Penning ionizing collisions that de-excite one metastable atom to the ground state and ionize the other.

The UCP is created from a two-photon ionization of the atoms in the MOT. The atoms are first placed in the $6p[5/2]_3$ state by the MOT beams, and then ionized by a pulse at 514 nm from a tunable pulsed dye laser. A pulse of 355 nm light from a frequency-tripled Nd:YAG laser provides a pump pulse (typically 10 ns, 200 mJ) to the dye laser. The dye laser uses circulating Coumarin 503 laser dye and the wavelength of the output pulse is controlled by adjusting the angle of a grating that

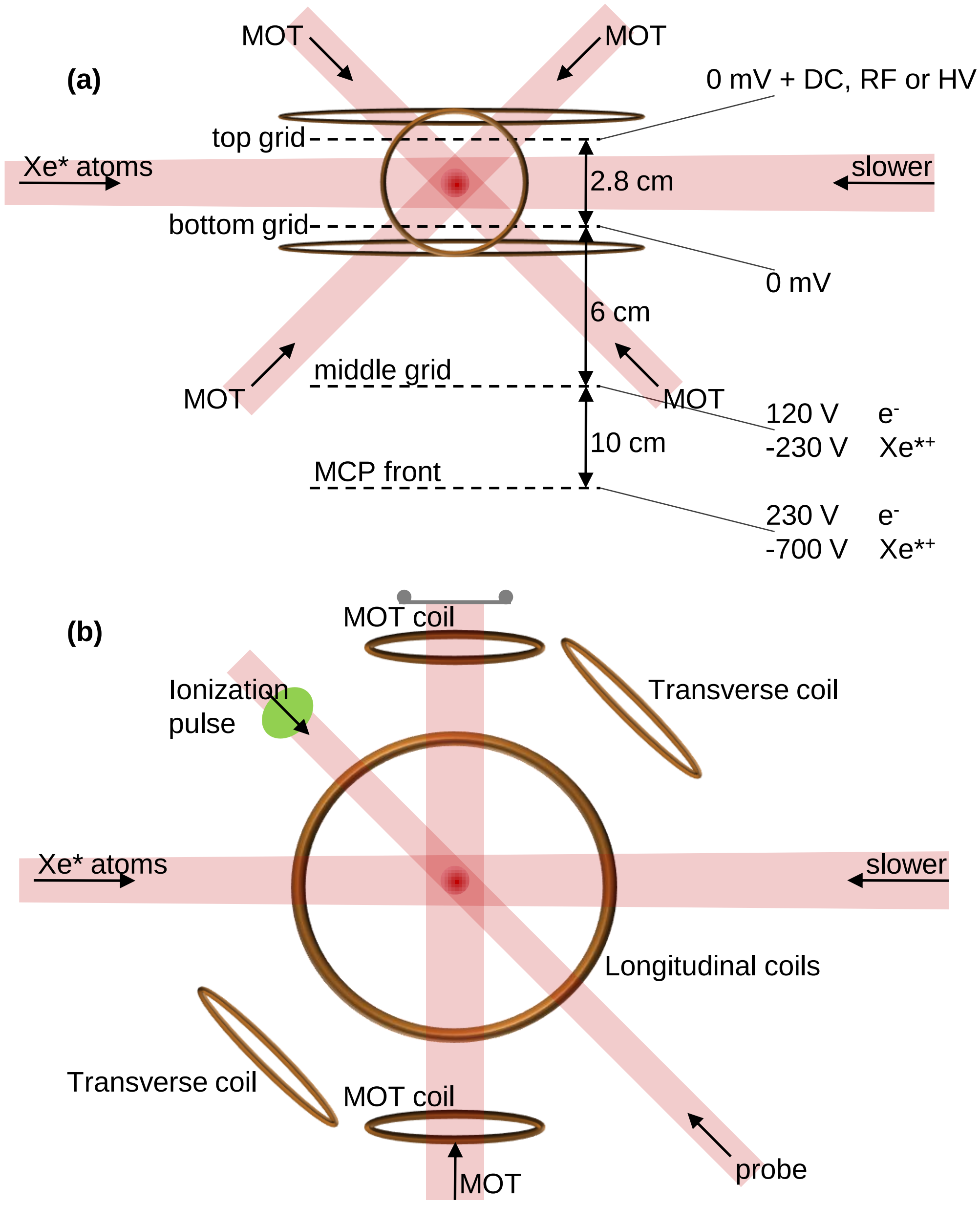

Figure 1.2: Vacuum chamber schematic. (a) Side View showing the grids with typical voltages for detecting the ion or electron current, the four MOT beams going through the grids, and the MOT and longitudinal coils. (b) Top View showing the three sets of coils used for magnetic field generation in the plasma and the location of the probe beam.

comprises one end of the oscillator cavity. Typical dye laser output is 1-7 mJ in a 10 ns pulse. We control the initial energy of the plasma electrons, E_e in Fig. 1.1, by adjusting the dye laser frequency relative to threshold in the range $E_e/k_b = 1-1000$ K. By tuning the laser below threshold, we can also excite the gas to specific high-n Rydberg levels.

After allowing the MOT to load, the MOT beams and magnetic field are turned off, and the cold atom cloud is allowed to expand for about 1.5 ms. The length of free expansion time is necessary for plasma experiments that require magnetic fields (Chapter 4). It may also help smooth out density fluctuations in the atom cloud that were caused by the intensity modulations in light from the MOT beams passing through the mesh grids. After this expansion period, the MOT beams are turned back on and the frequency set exactly on resonance a few μs before the fast ionizing pulse. The trapped atom cloud is small compared to the diameter of each of the MOT beams and the pulsed beam, so the intensity of ionizing light is roughly constant over the full Gaussian atom density. This makes the initial plasma density profile equal to the neutral atom density profile, although we do not observe significant changes in plasma dynamics even when the pulse beam is focused to a size comparable to the MOT. We can ionize a maximum of 30-40% of the atoms in the MOT, limited by the energy output of the pulsed laser. The number of atoms ionized is controlled through the laser power and the detuning of the MOT beams.

After the end of the plasma lifetime, the MOT is turned back on, in total ≤ 5 ms after it was turned off. All of the neutral atoms that were not ionized (70%) are still within the volume of the intersection of MOT beams, as the cold atoms cannot expand that far in 5 ms, and all of these atoms are re-trapped in the MOT. The time needed for the MOT to reload the lost atoms sets the lower limit of the experimental cycle at about 200 ms. The neutral atoms that are not ionized remain within the plasma volume through the plasma expansion, but we generally assume the neutrals to have no effect on the plasma, as the mean free path for charged particle-neutral atom collisions is much larger than the system size [4].

1.3 UCP Expansion

Most relevant to this work are the properties of the plasma during the expansion phase, after initial equilibrium has been established. This section outlines the ideal symmetric picture of expansion in the absence of external fields, and gives values of some relevant plasma parameters.

Conservation of energy and momentum during ionization results in the electrons taking nearly all of the excess energy in the laser photons (the ratio of ion kinetic energy to electron kinetic energy is approximately the mass ratio $m_e/m_i = 4 \times 10^{-6}$). We equate the excess photon energy, E_e, to the initial energy of the electrons. The electrons, having finite temperature, cannot be fully trapped in the plasma, and there is a prompt loss of electrons following plasma creation. The ions are stationary on this timescale, and electrons continue to leave until a large enough charge imbalance has built up to trap the remaining electrons. The magnitude of this initial electron loss is determined by the comparison of E_e to the confining energy of the developing plasma potential [4]. Ideally, after this initial loss during equilibration, the electron loss rate will decrease toward zero after a few μs as expected from simple evaporation. Thermal pressure from the remaining electrons will drive plasma expansion, without further loss. A more realistic version of this ideal picture is discussed in Chapter 2.

The self-similar Gaussian expansion of a UCP into vacuum has an exact analytical solution as long as the initial electron temperature is not too small ($T_e = 2E_e/3k_b > 50$ K), so that the heating effects of TBR can be ignored. In the limit that both species are weakly coupled, the ion and electron distribution functions, $f_{i,e}$, satisfy the Vlasov equation of kinetic plasma theory

$$\frac{\partial f_{i,e}}{\partial t} + \mathbf{v}\frac{\partial f_{i,e}}{\partial \mathbf{r}_{i,e}} - \frac{1}{m_{i,e}}\frac{\partial f_{i,e}}{\partial \mathbf{v}_{i,e}} q_{i,e} \frac{\partial \phi(\mathbf{r}_{i,e})}{\partial \mathbf{r}_{i,e}} = 0 \tag{1.2}$$

where the electric potential ϕ is given by Poisson's equation

$$\nabla^2 \phi(\mathbf{r}) = -e(n_i - n_e)/\epsilon_0 \tag{1.3}$$

The prompt electron loss ensures that the plasma is never perfectly neutral, but a key assumption needed to find a solution is quasi-neutrality, namely $(n_i - n_e) \ll n_i$. This should be satisfied in the bulk of the plasma, although it obviously fails near the edges. We can also take advantage of the fast equilibration times of the electrons compared to the ions, and assume the electrons to always be in quasi-equilibrium. They have an approximate Maxwell-Boltzmann velocity distribution and the time-dependence of this distribution is only in the temperature, $T_e(t)$. With these assumptions, a simple ansatz of a Gaussian density distribution for the ions

$$f_i \propto exp(\frac{-r^2}{2\sigma^2}) exp(\frac{m_i(\mathbf{v} - \mathbf{u})^2}{2k_b T_i}) \tag{1.4}$$

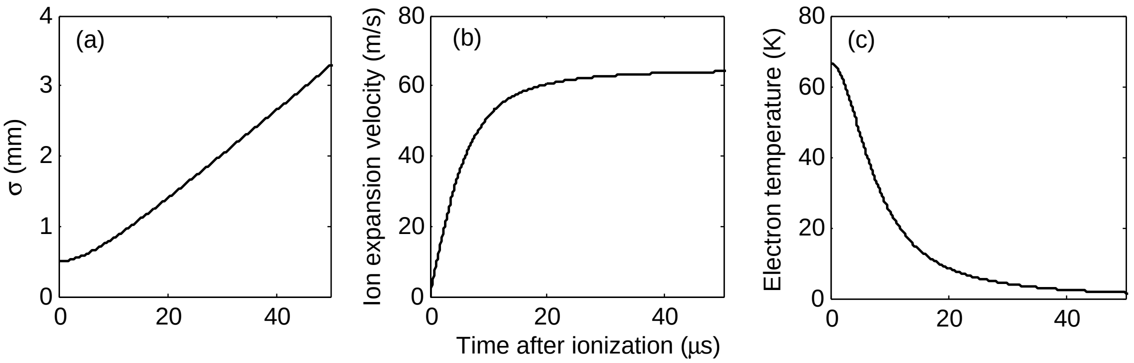

Figure 1.3: Plasma expansion. Time variation of (a) the rms radius, (b) the expansion velocity $u(r = \sigma)$ and (c) the electron temperature for $\sigma(0) = 500\ \mu$m and $T_e(0) = 67$ K.

can be shown [1] to satisfy the ionic kinetic equation, Eq. 1.2, with the following results for the ion density n_i, expansion velocity $\mathbf{u}(\mathbf{r}, t)$ and temperature $T_{i,e}$:

$$n_i(t) = \frac{N_i}{(2\pi\sigma^2(t))^{3/2}} e^{-r^2/(2\sigma^2(t))} \tag{1.5}$$

$$\sigma(t) = \sqrt{\sigma^2(0) + v_0^2 t^2} \tag{1.6}$$

$$\mathbf{u}(\mathbf{r}, t) = \frac{t v_0^2}{\sigma^2(t)} \mathbf{r} \tag{1.7}$$

$$T_{i,e}(t) = \frac{T_{i,e}(0)\sigma^2(0)}{\sigma^2(t)} \tag{1.8}$$

where

$$v_0 = \sqrt{k_b[T_e(0) + T_i(0)]/m_i} \approx \sqrt{k_b T_e(0)/m_i} \tag{1.9}$$

is the asymptotic expansion velocity. Fig. 1.3 shows the time evolution of σ, u and T_e for typical initial conditions in our experiments.

This model of expansion has also been studied in simulations [33–35] and has been confirmed in multiple experiments through measurements of the ion density

[22, 23, 36] and velocity [36]. The electron temperature evolution has been more difficult to measure, but experiments [21, 24, 37] have shown reasonable agreement.

The model fails when the initial electron temperature is tuned close to threshold. The rate of TBR scales as $n_e^2 T_e^{-9/2}$ [18–21]. For typical densities of plasma creation and initial electron temperatures of order 1 K, simulations [34, 35] and experiments [25] show that as much as 20% of of the plasma recombines via TBR to form Rydberg atoms. The energy released during recombination heats the plasma electrons to a temperature of 30-40 K, regardless of how low the initial temperature is set. Most of this heating happens quickly, and the UCP will subsequently expand at a rate roughly consistent with an initial temperature of 30-40 K, but the self-similar Gaussian expansion model does not match the experimental data as well as for higher temperatures [22, 36]. Section 2.3 contains further discussion of electron temperature measurements.

Even when $T_e(0) > 50$ K the temperature is not expected to decrease to an arbitrarily small value during the long 100-300 μs expansion time. Fletcher et. al. [21] used a measurement of the TBR rate to extract the electron temperature and found a scaling of $T_e \propto t^{-1.2}$ for times between 20 and 60 μs (the cooling rate is slower than the expected t^{-2} presumably due to TBR heating). When calculating plasma parameters (in the $T_e(0) > 50$ K limit), we generally use a model for T_e that follows the adiabatic cooling during the first $t_0 = 20$ μs and then scales as $t^{-1.2}$ at long times:

$$T_e = \begin{cases} T_e(0)[\sigma(0)/\sigma(t)]^2 & t < t_0 \\ T_e(t_0)[t/t_0]^{-1.2} & t > t_0 \end{cases} \tag{1.10}$$

The inhomogeneous density presents obvious challenges when considering characteristic plasma phenomenon such as plasma oscillations, Debye screening and collisional processes. For example, the local Debye length, defined as

$$\lambda_D(r) = \sqrt{\frac{\epsilon_0 k_b T_e}{n_e(r) e^2}} \tag{1.11}$$

is only about 10 μm at the center of the plasma at plasma creation, but it varies with the Gaussian density such that values of $\lambda_D(r)$ calculated near the edge of the plasma can be larger than the system size. But local definitions like this are not necessarily relevant as our experiments probe only global properties of the system. We will see in Chapter 3 an example of how the inhomogeneous density affects a global measurement of plasma oscillations. Figure 1.4 shows some typical values of the plasma frequency, Debye length and electron thermalization time using the central plasma density. The plasma frequency is

$$\omega_p(0) = \sqrt{\frac{e^2 n_e(0)}{\epsilon_0 m_e}} \tag{1.12}$$

The thermalization time is calculated from the standard electron self-collision time [38]

$$t_{ce} = \frac{2\pi \epsilon_0^2 m_e^{1/2} (3 k_b T_e)^{3/2}}{0.714 n_e e^4 \ln(\Lambda_e)} \tag{1.13}$$

where $\ln(\Lambda_e) = \ln(3\sqrt{2}\pi\lambda_D^3 n)$ is the Coulomb logarithm.

1.4 Diagnostics of UCPs

Ultracold plasmas are small systems, consisting of only $10^4 - 10^9$ ions and electrons and sizes of 0.1mm to 1cm, and available probes of UCPs have been limited.

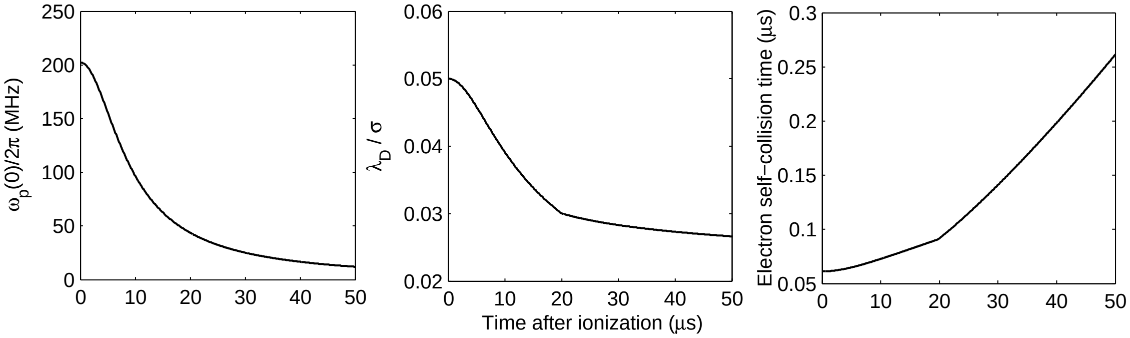

Figure 1.4: Plasma properties. Time variation of (a) the plasma frequency, (b) the Debye length and (c) the electron thermalization time for $\sigma_0 = 500$ μm and $T_e(0) = 67$ K. The kinks at 20 μs in (b) and (c) reflect the change in the functional form of T_e.

The small size prevents the use of conventional electric probes placed inside the plasma. Great success has been found in using *in situ* optical imaging of the plasma ions, but these methods are not practical for all ion species. The primary diagnostic in our lab is charged particle detection. The grids in our vacuum chamber allow us to easily monitor the natural loss of electrons or ions from the plasma. We can also destructively image the plasma ion or electron distribution by projecting the spatial distribution onto the detector. In this section, we summarize the various charged particle diagnostics available in our system and a new diagnostic where we non-destructively detect oscillations of the plasma through the induced current on nearby electrodes.

1.4.1 Electron Current

Our UCPs are created between two wire mesh grids, 2.8 cm apart. In typical experiments, we apply a small voltage difference of about 30 mV between the grids.

The small electric field is needed to direct escaping electrons through the bottom grid, after which they are accelerated through a third grid and onto a microchannel plate detector (MCP). The grid positions and typical accelerating voltages are shown in Fig. 1.2.

The flux of electrons striking the MCP is amplified and recorded and a typical electron current signal is shown in Fig. 1.5. There is a sharp peak immediately following plasma creation that corresponds to the initial loss of electrons during equilibration. During the expansion phase, electron evaporation produces the broad feature.

Electron detection has been used to measure a wide array of plasma phenomenon including collective oscillations of the plasma [22, 39], Rydberg atom formation [21, 25], plasma instabilities [26], and electron temperature [21, 24]. All of these measurements involved applying perturbing fields, from dc pulses to microwaves, and observing the change in the electron emission. Electron detection has also been a main diagnostic in studies of the spontaneous evolution of Rydberg gases into plasmas [5, 6], the demonstration of a molecular UCP [9] and of a UCP in a strong magnetic trap [40]. Despite all of this work, the broad feature of the unperturbed electron emission signal has not been previously explained. In section 2.2 we present a model that can reproduce this feature by calculating the rate of forced electron evaporation due to the externally applied electric field.

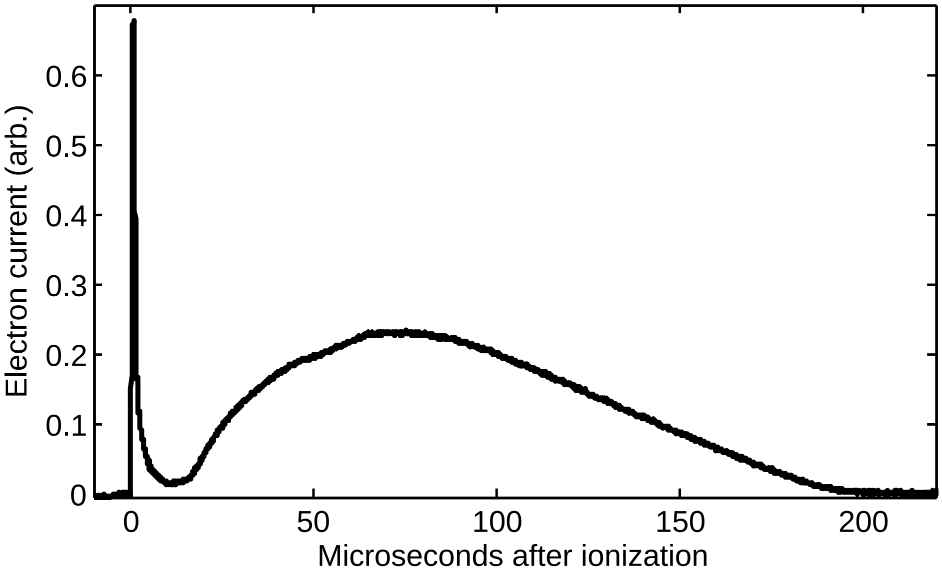

Figure 1.5: Electron current signal. An example electron current signal with plasma parameters $E_e/k_b = 100$ K, $N_i = 1.0 \times 10^6$ and an applied electric field of $E_{ext} = 10$ mV/cm.

1.4.2 Ion Current

Similar to collecting the electron current, we can simply reverse the voltages on the accelerating grids and collect the ion current. Figure 1.6 shows a typical ion current signal. We understand the shape of the signal by considering the self-similar expansion of a Gaussian ion distribution with its center fixed at the mid-point between the grids. The ion current should be equal to the flux of ions that pass through the circular planar grid of radius R, as depicted in Fig. 1.6. Ions outside of this conical region do not get accelerated to the detector, as they either strike the solid ring electrode that holds the mesh grid or continue expanding into empty regions of the vacuum chamber.

Given the time-varying ion density (Eq. 1.5), the number of ions that have passed through the circular grid aperture is

$$N_{out}(t) = 2\pi \int_{\theta=0}^{\beta} \int_{r=d/cos\theta}^{\infty} n_i(t,r) r^2 sin\theta \; d\theta \; dr \tag{1.14}$$

where $\beta = \tan^{-1}(R/d)$ and the ion current is simply dN_{out}/dt. Fig. 1.6 shows the comparison of the calculated ion current with the measured signal. The ions have a time of flight of 7.5 μs between the bottom grid and the detector (for typical voltages given in Fig. 1.2), but this delay has been subtracted from the data signal so that the time axis represents the time at which ions cross the bottom grid.

Despite the simplicity of this measurement it has not been studied prior to this thesis. In Chapter 4 we will show ion signal measurements of the plasma expansion for different parameters and discuss the quality of the Gaussian density approximation. The ion signal is also useful in understanding the plasma expansion

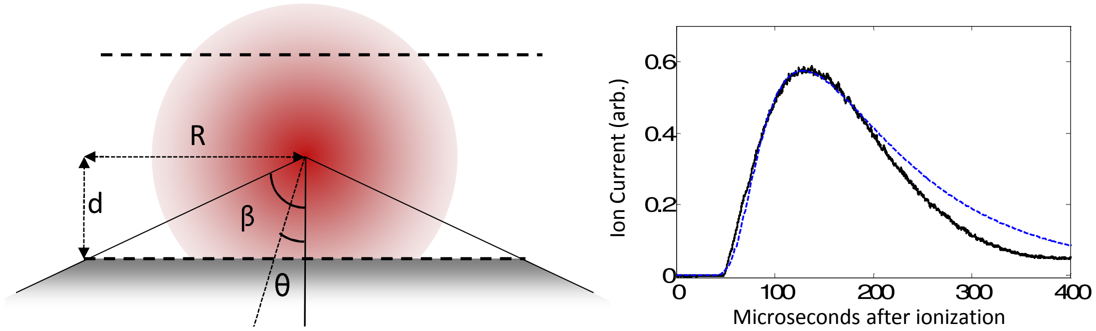

Figure 1.6: Ion current signal. (Left) Schematic of a Gaussian ion distribution expanding through the planar grid. In our setup, $d = 14$ mm and $R \approx 40$ mm. (Right) Measured ion current signal (solid black) compared to calculation (dashed blue) for a plasma with $E_e/k_b = 100$K. Calculation is a fit to the data between 0 and 200 μs, giving $v_0 = 75$ m/s.

in magnetic fields.

1.4.3 Ion Projection Imaging

We can also use the MCP to take projection images of the ion density. Our MCP is equipped with a phosphor screen that allows for spatial imaging of the charges striking the MCP surface. During plasma expansion, we apply a high voltage pulse to the top grid that immediately removes all of the electrons from the plasma and accelerates the ions toward the MCP. The MCP magnifies the signal and we take an image of the illuminated phosphor screen with a ccd camera. By applying the voltage pulse at varying times, we can track the expansion of the plasma.

To properly relate these images to the ion distribution in the plasma, we must consider the ion dynamics during the time-of-flight to the detector, including Coulomb explosion of the ion space charge and lensing from the electrode geometry.

We must also be careful to eliminate background signals from ions that escape the plasma prior to the application of the imaging voltage pulse.

The initial setup for projection imaging in our apparatus is described in the thesis of Xianli Zhang [30] and was used in measurements of the plasma expansion transverse to a uniform magnetic field [23, 41]. In Chapter 4 we give a detailed analysis of ion projection images and show new measurements of plasma expansion both parallel and perpendicular to a uniform magnetic field, and of expansion in a cusp field.

1.4.4 RF Mode Detection

Traditional laboratory plasmas have long used plasma oscillations and other collective modes as diagnostic tools. Plasma oscillations have been observed in UCPs [22] by observing an enhancement in the electron current signal in response to an applied rf field. But we can also use a more traditional approach of detecting oscillations by monitoring changes in the applied rf field. In our system, this involves applying an rf field to the top grid and monitoring changes in the rf field received on the bottom grid. The oscillations in the plasma induce a current on the bottom grid that is large enough for us to measure, despite the small number of particles in the plasma.

In Chapter 3 we describe the electronic mode detection and the advantages it provides over charged particle detection, and use it to detect various electrostatic electron oscillations.

1.4.5 Other Probes

Optical absorption and fluorescence imaging of the plasma ions is a powerful diagnostic. Unfortunately, the lowest energy transition from the ground state of the Xe^{*+} ion corresponds to a 124 nm photon, which is too far in the UV for ion imaging to be practical in our system. Studies of Sr and Ca UCPs have used both absorption [7] and fluorescence [8] techniques (at optical wavelengths between 400 nm and 500 nm) as *in situ* measurements of the spatial density and velocity distributions of the ions. This has allowed for detailed measurements of the ion expansion and the observation of ion acoustic waves resulting from the imprinting of density modulations [16, 17]. The ability to also measure ion velocity has given information on the DIH process [13–15], and may also allow measurements of the ion collision rates [42, 43]. Of course, optical probes detect the ions, so information about the electrons can be obtained only indirectly through their effect on the ions [37].

UCP expansion has also been measured recently through spectroscopic detection of the plasma electric field [44]. This is done through the associated Stark shift of a microwave transition between two high-n states of Rydberg atoms embedded into the plasma.

1.5 Related Work

1.5.1 Plasmas formed from Rydberg Gases

Ultracold plasmas can also be formed by tuning the frequency of the ionization laser just below threshold, creating a dense cloud of highly excited Rydberg atoms [5, 6, 45–50]. If the Rydberg atom density is large enough, the atoms will spontaneously ionize to form an UCP with properties very similar to those that were created by direct ionization just above threshold. The spontaneous ionization starts either from blackbody ionization of Rydbergs or when interactions between the Rydbergs lead to Penning ionization of Rydberg pairs. If enough atoms are ionized that a small plasma can form, then the electrons in that plasma collisionally ionize more Rydbergs starting an avalanche process that ionizes the majority of the Rydberg gas (to conserve energy, some fraction of the Rydbergs get transferred to deeply bound states). The importance of interactions between Rydberg atoms in driving this ionization is closely related to the recent interest in using these strong interactions as gates in a neutral atom based quantum computer [51] or for the study of quantum many-body physics [52–54].

UCPs have also been created from the spontaneous ionization of a molecular Rydberg gas [9, 55]. As the ion temperature in UCPs formed from a MOT increases dramatically from the MOT temperature to about 1 K after creation, the ionization of a sample of atoms or molecules cooled only to 1 K temperatures may produce the same physics. In a supersonic molecular beam, polar molecules are routinely translationally and rotationally cooled to this level (in the rest frame of the beam).

The molecules can then be ionized above threshold or excited to Rydberg states to form a plasma.

This experiment has been done with a molecular beam of NO molecules [9]. The high-density of the molecular beam allows for a denser plasma than those created from a MOT, although the molecular plasma has been shown to undergo a fast decay possibly due to dissociative recombination of the molecules [56–58]. The expansion velocity of these ultracold molecular plasmas has also been measured, and found to be surprisingly small [55]. Assuming the expansion follows the same self-similar equation used for atomic UCPs, the initial electron temperatures would be < 10 K, small enough that the electron coupling constant would be $\Gamma_e > 1$, given the molecular beam density. The prospect of strongly coupled electrons is interesting, but would require a suppression of DIH and TBR that is not understood, and skepticism remains about the validity of the strong coupling claim [20, 59]. Still, the success of these experiments opens up the study of UCPs to the wide array of species that can be cooled in a molecular beam and allows the study of UCP dynamics with the addition of molecular degrees of freedom and recombination.

1.5.2 One-component Plasmas and Antihydrogen Production

Plasmas composed of particles with a single sign of charge, or one-component plasmas (OCPs), can be stably trapped, usually in Penning traps. Studies of OCPs have a history in both atomic and plasma physics [60, 61]. They have drawn interest because they are trapped and easily controlled systems in a state of global thermal equilibrium [62] and still display a range of collective plasma phenomena. OCPs of ions can be laser-cooled to the point of crystalization, making them ideal systems for the study of strong correlations [63, 64]. Although created in a trap with a strong magnetic field and external electric potential, the OCPs have similar size and density to our neutral plasmas, and thus the available diagnostics are similar. In Chapter 3 we will relate our new rf mode diagnostic to similar work previously done with trapped OCPs.

Efforts to create and trap antihydrogen atoms start with separate Penning traps holding OCPs of positrons and anti-protons before bringing them together to form a neutral plasma. Anti-hydrogen atoms are primarily formed in high-n Rydberg states via TBR in the plasma, as in our UCP. Recently, this method has succeeded in trapping a small number of anti-hydrogen atoms for up to 1000 s [65, 66] and future work is aimed at spectroscopy of ground state anti-hydrogen.

1.5.3 Ultracold Electron and Ion Sources

The photo-ionization of laser-cooled atoms can also be used for the generation of low-emittance ion and electron beams. Inspired by work on UCPs, Claessens *et al.* proposed in 2005 to use them as a source for cold electrons [67], followed by a similar proposal for an ion source [68]. Ion beams and electron beams have wide use in imaging and fabrication technologies that require the beams to be focused to ever-smaller spot sizes. A key limiting factor in the achievable spot size is the transverse velocity spread of the particles at the source. Ultracold atoms ionized near threshold offer a source with ion and electron temperatures orders of magnitude lower than state-of-the-art sources. An additional advantage of MOT ion sources is that any element capable of being laser-cooled can be used.

Recent experiments have begun to realize this capability [69–72]. Both pulsed and continuous sources can be created. For a pulsed source, a MOT is loaded and then all (or a significant percentage) of the atoms are ionized, as in our ultracold plasma experiments. The atoms are typically ionized in the presence of a strong electric field that immediately separates the charges such that plasma dynamics are unimportant. For a continuous source, a MOT is continuously ionized, but at a rate slower than the MOT loading rate. Ultracold electron and ion sources represent a promising application of laser-cooling physics.

1.5.4 Atomic Clusters

Plasmas formed by high-energy laser irradiation of solids, films or clusters can also have strong correlation effects and undergo expansion into vacuum. Laser-produced plasmas often have solid densities, so the characteristic time-scale for electron motion, which scales as $w_p^{-1} \propto n^{-1/2}$, is on the order of attoseconds. UCPs have much lower temperatures and densities and offer a chance to study some of the same physics at more experimentally accessible time-scales [73]. Of particular similarity are atomic clusters, spheres of 10^2 to 10^7 atoms at near solid densities [74]. Ionization of clusters with high-energy femtosecond laser pulses has produced harmonic generation [75], high-energy ions [76] and laser pulse self-focusing [77]. In

Chapter 2, we borrow from previous theoretical work on atomic clusters to calculate the electron spatial distribution in our UCP.

Chapter 2

Electron Distribution

2.1 Overview

The electron distribution function of a UCP has received a great deal of theoretical attention [35, 78–80], but the inability to use electric probes inside the plasma makes experimental verification of both the position and velocity space distribution difficult. All UCP theory prior to this thesis has assumed the plasma has complete spherical symmetry. This assumption seems reasonable as the initial spatial distribution comes from an atomic cloud with a spherically symmetric Gaussian distribution, and there are no large external electric or magnetic fields applied to the system in most experiments. But in order to facilitate good electron detection in our system, we do apply a small external electric field. We have found that this field creates an asymmetry in the plasma that has significance to the electron spatial distribution and the observed electron current signals. Additionally, our plasma is a finite system with open boundary conditions, so the electron velocity distribution cannot follow a true Maxwell-Boltzmann form, leading to predictions of a Michie-King distribution [79, 80], which has been developed for gravitationally bound systems in astrophysics. Previous experimental work has focused only on measuring the global electron temperature [21, 24, 37], which is changing dynamically during expansion from the competition of adiabatic and evaporative cooling with three-body recombination heating.

In this chapter, we present an introduction to the spatial and thermal distribution of electrons in the plasma and the process of electron evaporation during the plasma expansion. We present two theoretical models that take into account the asymmetry introduced by an applied electric field and show that these can be used to explain the observed rate of electron emission from the plasma [81], which was not previously understood. We briefly discuss previous measurements of the electron temperature and prospects for measuring the thermal distribution.

Figure 1.5 shows a typical emission curve from our experiment over the entire lifetime of the plasma, showing the prompt peak of electrons emitted during plasma formation, followed by electrons continuously emitted during the expansion phase. In principle, this signal contains information about the electron distribution and evaporation processes. At a given time, each electron is bound to the plasma in a potential well of finite depth, created by the combination of the slow-moving ion cloud, the applied electric field and the other electrons. Since the electron collision times are short compared to the plasma expansion, electrons will evaporate out of the plasma until a quasi-equilibrium is established. Of course, the trapping potential is the full potential of the plasma which depends on the electron number; for each electron lost, the plasma potential well binding the remaining electrons deepens.

In the case of perfect spherical symmetry and no external fields, the predicted electron evaporation rate becomes exponentially small as the plasma expands, due primarily to the fast decrease in the electron temperature, due to adiabatic cooling. We calculate this by numerically finding a self-consistent solution to Poisson's equa-

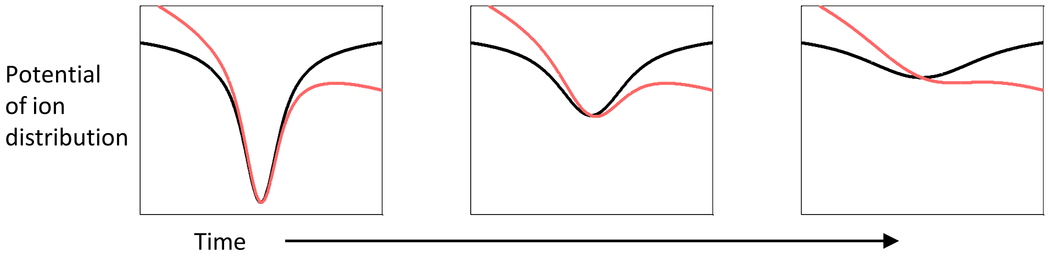

Figure 2.1: Electric potential of the ion distribution. The black curves show the potential from ions at increasing times during expansion with no applied fields. The red curves show the potential with the addition of a constant uniform electric field.

tion, the details of which are explained in Sec. 2.3. If we assume the electron temperature is decreasing following adiabatic expansion $T_e \propto \sigma^{-2}$ (the deviation from a Maxwell-Boltzmann distribution is mostly in the high-energy tail, so T_e should still be a good parameter), ignore three-body heating and assume no electron loss, the self-consistent solution gives us the depth of the plasma potential well. The relevant parameter for evaporation is the relative depth of the potential compared to the electron temperature, $\eta = \phi(r = 0)/k_b T_e$. The result is that η increases as the plasma expands, meaning the evaporation ceases after the initial loss. The rate of initial evaporation from the plasma was simulated by Robicheaux using a Monte Carlo method [34] and found to be in good agreement with the observed prompt peak in our electron emission signal.

The reason that we see any electron loss past the prompt peak is entirely due to the presence of the external electric field. As the density decreases from expansion, the external field can penetrate farther into the plasma, spilling more electrons and forcing the evaporation to continue. If we consider only the ion distribution and external field, as in Fig. 2.1, it is easy to see how the potential from the external field becomes greater than the potential from the ions and forces gradual electron loss even in the limit of zero electron temperature. The observed lifetime of the broad peak in the electron signal is directly related to the strength of the applied field, and ultimately the maximum achievable lifetimes are set by stray fields in our vacuum chamber (although even in the absence of stray fields, the plasma expansion sets a practical limit on the lifetime).

2.2 Zero Temperature

2.2.1 Spatial Distribution

We can separate the effects of the external electric field on electron emission from the effects of thermal evaporation by using a zero-temperature model. We find that this consideration alone can reproduce the basic shape of the electron emission curve. We present an electrostatic calculation that gives the zero-temperature electron spatial distribution for a stationary ion density and applied field. This gives the maximum number of electrons that can be held in the plasma in the absence of evaporation. Applying this calculation at all times during expansion allows us to predict the flux of cold electrons from the plasma, which we find is in excellent agreement with the observed electron signal.

We consider experiments where an UCP is created with large initial electron energy and undergoes self-similar Gaussian expansion. As the plasma expands, the electron and ion densities decrease and the electron temperature decreases according to Eq. 1.8. The combined effect means the thermalization time for electrons steadily increases but remain less than a μs over the entire plasma lifetime (Fig. 1.4). This allows us to assume that the electrons maintain a quasi-equilibrium within the continually decreasing potential well. A constant electric field of 0 - 200 mV/cm is applied between the top and bottom grid to obtain electron signals similar to Fig. 1.5.

For our calculation, we first consider a fixed point in time and allow the electrons to move and establish equilibrium within the stationary ion density. An example of a Gaussian ion cloud tipped by a uniform external field is shown in Fig. 2.2(b) (dashed curve). We treat the electrons as a zero-temperature fluid, and seek the maximum number of electrons such a potential can hold and the resulting spatial distribution. The zero-temperature approximation requires a net zero electric force on all electrons in equilibrium, so the maximum number of electrons can be determined by adding electrons until the combined electron and ion potential becomes flat [Fig. 2.2(b) (solid curve)]. In the absence of an external field, the solution is an electron density that exactly matches the ion density everywhere in space. But an external field reduces the number of electrons that can be held, pushing the extracted electrons away from the system. The electron density will still exactly match the ion density in some region of space with a sharp boundary and be zero outside that boundary. The shape of the boundary is defined such that the ion density outside the boundary has the correct shape to exactly cancel the external field everywhere within the electron cloud, resulting in a net zero force on all electrons.

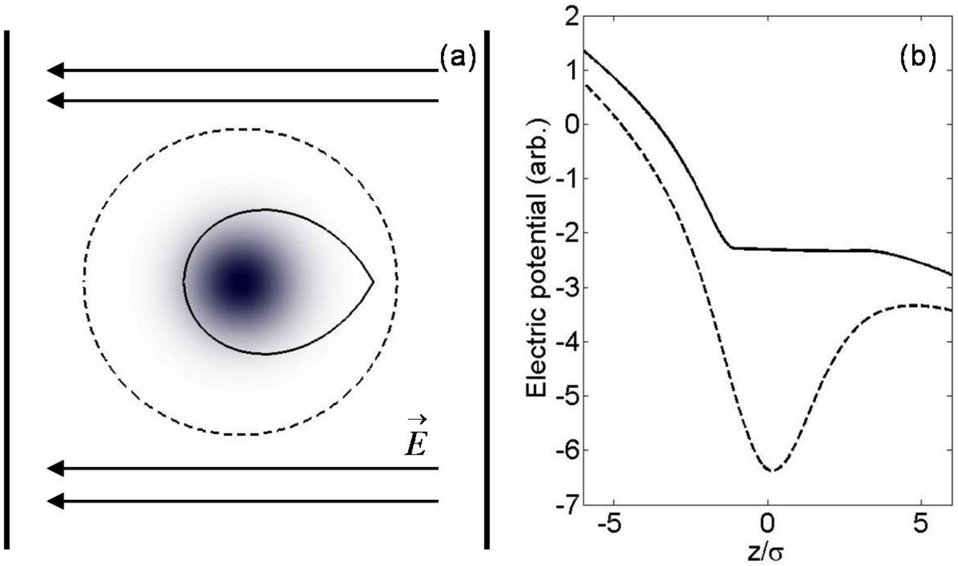

Figure 2.2: Electron cloud schematic. (a) A schematic of our setup including a contour plot of ion density and electric grids. The solid line shows the sharp edge of the cold electron cloud, and the dashed line is the 3σ radius of ion cloud. (b) The potential along the symmetry axis due to (i) the ion distribution plus external field (dashed) and (ii) the total distribution including cold electrons (solid).

To find the proper shape of the electron cloud, we use a numerical algorithm first used by B. Breizman and A. Arefiev to analyze a similar problem in laser-irradiated cluster physics [82, 83]. There are many similarities that can be drawn between laser-irradiated clusters and UCPs [73], as both systems are finite unconfined plasmas created from laser ionization, despite the huge difference in the absolute densities and temperatures.

We define a boundary to the electron cloud that is initially at the edge of the ion distribution. We take the ion density to be a Gaussian with a cutoff at 3σ. The cutoff is a practical necessity for the numerical algorithm, but it also reflects the predicted existence of a small ion density spike near the 3σ point of the expanding plasma that arises from the initial charge imbalance [34, 35]. We calculate the electric field at the boundary and then displace the boundary by an amount proportional to the local value of the field. After repeating this process over many iterations, the boundary motion slows down and eventually stops as it reaches the case of zero field at all boundary points. Inside the boundary the electron density exactly matches that of the Gaussian ions and the integration of this gives the total electron number. Examples of the electron boundary shape are given in Fig. 2.3. We have not been able to find an analytic solution for these curves. Some details of the numerical algorithm are given in Appendix A.

We perform this calculation at all times during expansion, assuming the ion cloud center is fixed and the size follows the ideal self-similar expansion. As the density decreases, the electric field has a stronger polarizing effect such that fewer and fewer cold electrons can be held in by the ions. Eventually the density is

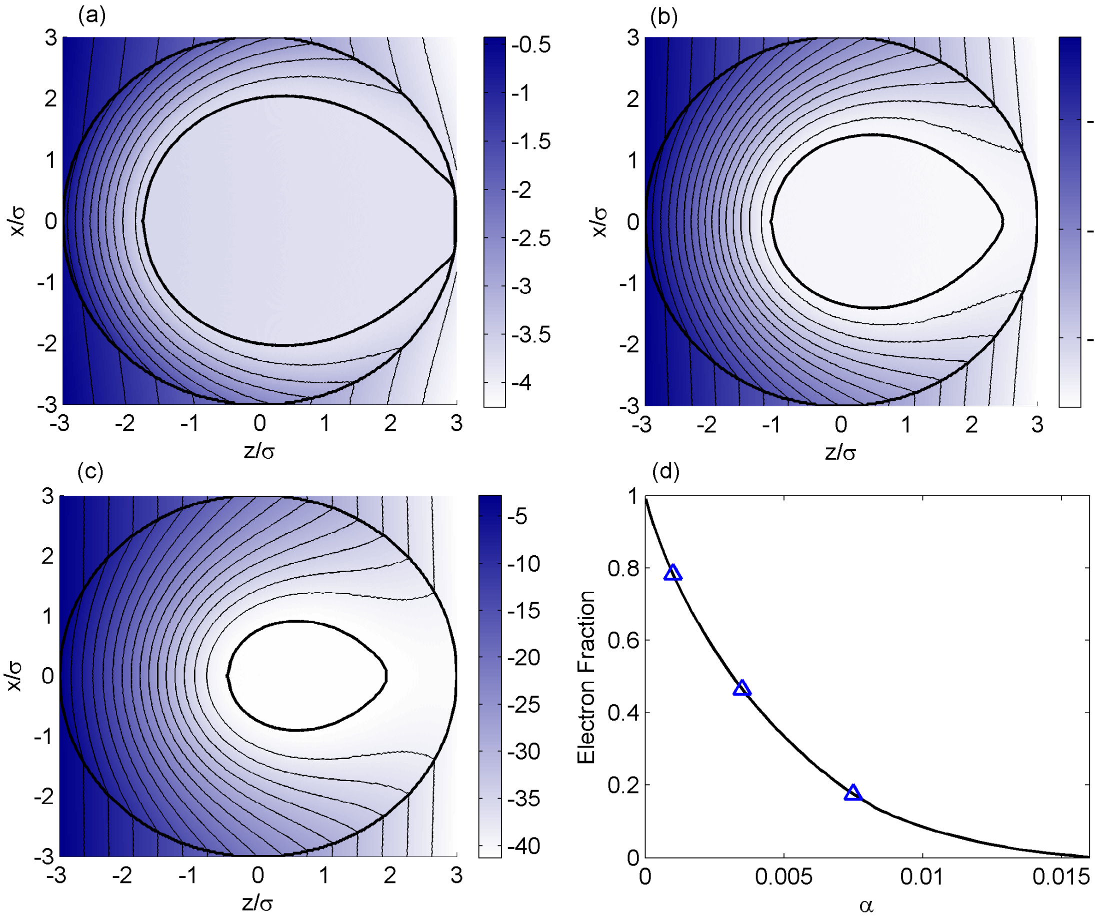

Figure 2.3: Electric potential of plasma in a uniform electric field. (a)-(c) Potential maps of the plasma showing lines of equipotential for $\alpha = 0.001$, $\alpha = 0.0035$ and $\alpha = 0.0075$ respectively. The thick solid lines are the boundaries of the ion and electron clouds. The potential is constant everywhere inside the electron cloud boundary. The color scales all have the same arbitrary units. (d) The calculated electron fraction for all α. The triangles indicate the results shown in (a)-(c).

low enough that the electric field dumps all electrons. We calculate the maximum number of cold electrons as a function of time (ion density).

The shape of the boundary and the fraction of electrons to ions, N_e/N_i, depends only on the ratio of the external field, E_{ext}, to the characteristic field of the ions. We find N_e/N_i for one set of dimensionless values of

$$\alpha = \frac{E_{ext}\epsilon_0\sigma^2}{eN_i} \tag{2.1}$$

where N_i is the number of ions. The electron fraction N_e/N_i decreases monotonically for increasing strength of α; the results are shown in Fig. 2.3(d).

2.2.2 Electron Fraction

Figure 2.4(b) shows the measured fraction of electrons in the plasma as a function of time, found by integrating the electron signal in Fig. 2.4(a), and the corresponding calculated cold electron fraction from our model. The calculation predicts the general shape and timescale of the signal over a wide range of initial parameters. As expected, the calculation overestimates the plasma neutrality during the prompt loss of thermal electrons, the discrepancy greater for higher E_e and lower N_i [4]. For the data in Fig. 2.4, the expansion velocity of the plasma is measured using a fit to the ion current signal (as in Fig. 1.6), and the number of plasma ions is left as a fit parameter in order to show how well the shape of the zero temperature theory matches our data. The expansion velocity and ion number are sufficient to calculate the value of α as a function of time and thus the theoretical electron fraction as a function of time.

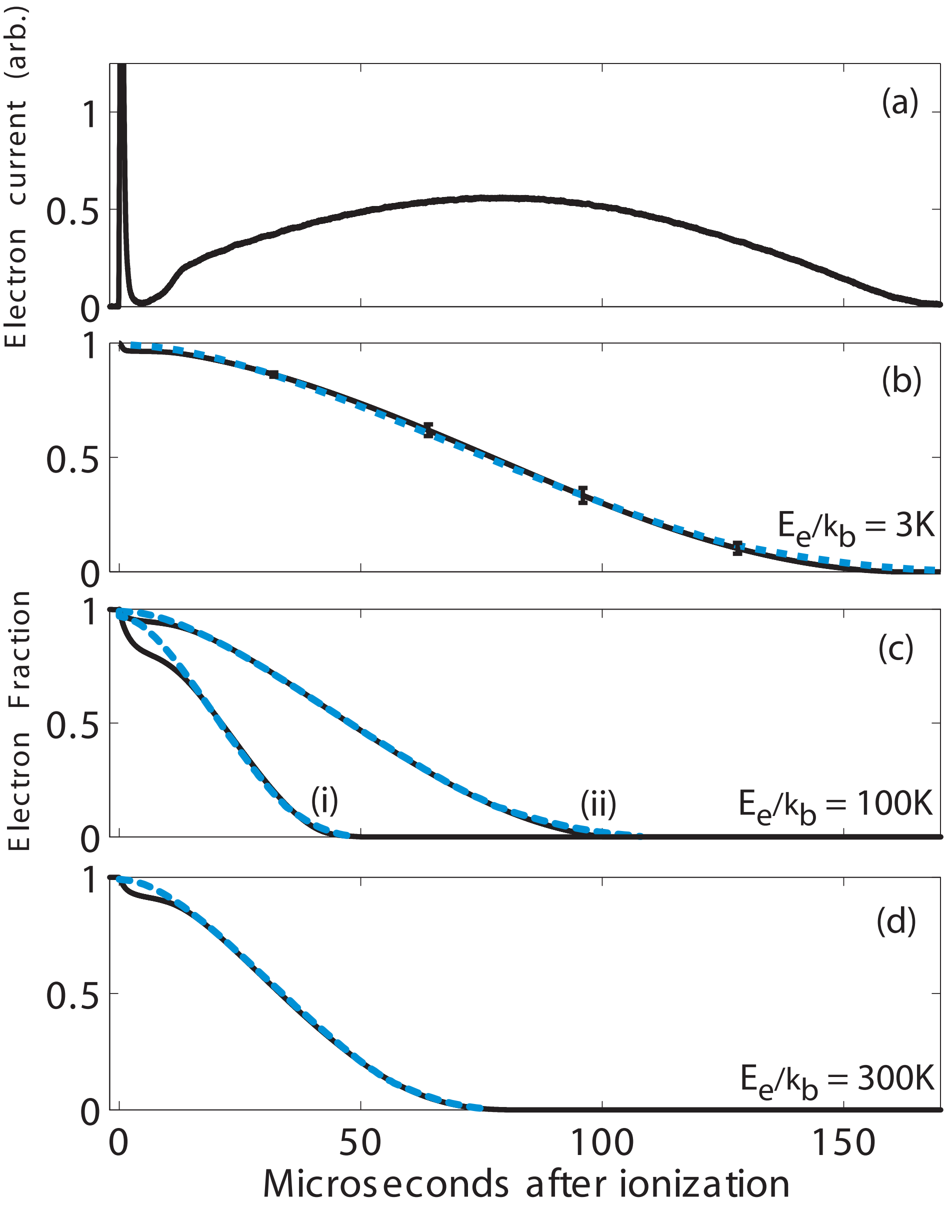

Figure 2.4: Cold electron fraction. (a) An example electron current signal. (b)-(d) The integrated data signal (black solid) compared to theory (blue dashed) with E_{ext} = 50 mV/cm. Neutrality curve in (b) corresponds to the electron signal in (a). Plasma parameters are (b) $N_i = 1.1 \times 10^6, v_0 = 47$m/s, (c,i) $N_i = 0.23 \times 10^6, v_0 = 75$m/s, (c,ii) $N_i = 1.0 \times 10^6, v_0 = 70$m/s, and (d) $N_i = 0.92 \times 10^6, v_0 = 95$m/s. Electron signals are the average of 50 shots with characteristic statistical uncertainty shown in (b).

Figure 2.5 shows a direct comparison of data taken with different strengths of electric field. Stronger fields shorten the plasma lifetime, but plotting the signals using our normalized coordinate α shows a similar rate of electron loss for all. Electron signals taken for varied initial density and initial electron energy are also found to follow this universal curve. For initial energies below $E_e/k_b \approx 60$ K the shape of the observed signals does not match as well to the theory. At these low temperatures, an increased TBR rate converts as much as 15% of the plasma ions into Rydberg atoms [34, 35] (our calculation has assumed a constant ion number), and the model of self-similar Gaussian expansion is less accurate [37].

Late in its lifetime, the plasma is large enough for the edges of the ion cloud to start crossing the mesh grids. By monitoring the ion current signal, we determine that the first ions start crossing the grid when the grid position is between 3 $\sigma(t)$ and 4 $\sigma(t)$. The ion signal also shows a sharp turn-on, indicating a sharp edge to the ion density, which supports our assumption of a Gaussian density with a sharp drop at $\approx$3 σ. For times after this, a more correct density might be a Gaussian with a planar cut-off at the locations of the grids. In Fig. 2.5(b), we compare only the times before the ions start crossing the grid. Practically this makes little difference, as the grids only cut off the low density outer regions of the plasma. We have performed the cold electron calculation with the grids included for a large and slow (9×10^5 ions and $v_0 = 60$ m/s) plasma with a low electric field (15 mV/cm), where the lifetime is long. The result gives lower neutrality for all times after the plasma starts crossing the grid, but the differences are less than 5 percent compared to the case where we ignore the grids. But this is still ignoring the influence of ions crossing

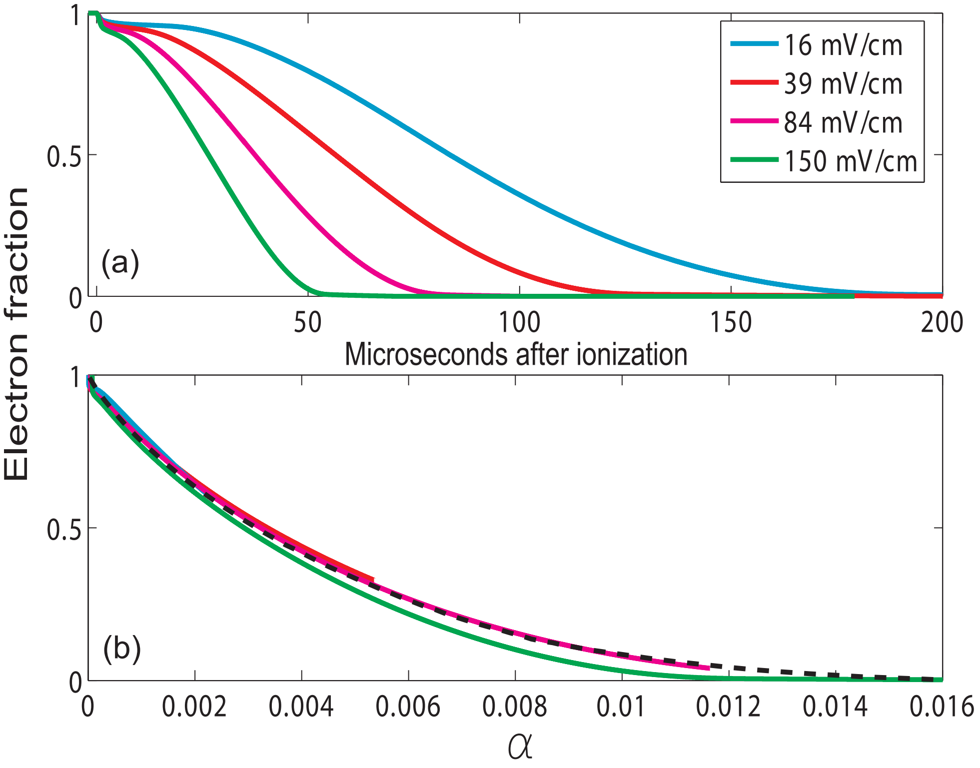

Figure 2.5: Universal scaling of electron signal. (a) Integrated electron signals for varied external field, and (b) the same signals plotted vs the normalized α. The black dashed line is the theoretical result. Data signals are the average of 50 shots with $E_e/k_b = 100$ K and $N_i = 1 \times 10^6$. The ion cloud starts crossing the grids at 71 μs.

the bottom grid that get reflected back into the plasma since the accelerating fields are set to select electrons. In general, the fits to theory are best when the electron signal lifetime is less than 120 μs.

Above 200 mV/cm, the signal scaled with α begins to diverge from the universal curve seen in Fig. 2.5(b). For strong fields, the neutrality drops quickly enough that it alters the ion expansion, both from the linear acceleration of free ions in the applied field and from the Coulomb repulsion between the ions. The Gaussian density approximation then becomes invalid. Residual electric fields in our vacuum chamber prevent application of an arbitrarily small field, and ultimately limit the maximum observable plasma lifetime. Stray fields along the grid axis can be canceled with slight adjustments to the grid voltages. We monitor the total number of electrons detected over the full lifetime and see a drop from all electrons detected to none as one grid voltage is changed over a 25 mV range. The midpoint of this transition should be close to zero axial field and typically comes with a 20-30 mV difference between the grids. This difference is taken into account in our reported field values. Stray transverse fields are not canceled, but we estimate them to be no greater than 15 mV/cm based on the quality of our fits near zero axial field.

2.3 Finite Temperature

We now discuss the thermal distribution of electrons in the plasma. We first discuss the expected form of the thermal distribution and previous measurements of the global electron temperature. We then present a self-consistent solution of

Poisson's equation for our plasma including the external electric field. We use this to again calculate how the electron fraction changes during the plasma expansion and find only small corrections to the zero temperature solution, which should be expected given the success of the zero-temperature approximation and the universal character of the electron signal.

2.3.1 Michie-King Distribution

Because the plasma electrons are held in a finite-depth trap, a true Maxwell-Boltzmann distribution cannot exist, as highly energetic electrons can not be held in the trap. Instead, we will use a Michie-King (MK) distribution, which is simply a Maxwell-Boltzmann distribution with a constant subtracted to make the distribution go smoothly to zero at the maximum energy of the trap:

$$f \propto (e^{-(E-E_t)/k_b T_e} - 1)\Theta(E - E_t) \tag{2.2}$$

where E is the electron energy, E_t is the trap depth and Θ is the step function. This distribution was originally developed in the study of globular star clusters [84, 85]. Like electrons in UCPs, star clusters are open systems that typically have a Gaussian density distribution and a small $(10^3 - 10^7)$ number of particles that interact via $1/r^2$ forces, with the obvious difference of attractive interactions.

The analogy to gravitationally bound star clusters was first pointed out in one of the original theoretical studies of UCPs by Kuzmin and O'Neil [10, 11], where the authors borrowed existing computer codes originally developed for the study of binary star formation in star clusters and modified them to be applied to UCPs.

A detailed analysis of the comparison and how equations for gravitationally bound systems can be modified for UCPs was done by Comparat *et al* [79].

It is natural for us to contrast this evaporation to a similar system in quasi-equilibrium familiar in atomic physics: trapped ultracold atoms undergoing forced evaporation for the production of Bose-Einstein condensates. In the atomic case, a Boltzmann distribution with a hard truncation at the trap depth is generally assumed:

$$f \propto e^{-(E-E_t)/k_b T_e} \Theta(E-E_t) \tag{2.3}$$

The reason for the different distributions arises from the difference in the type of collisions. A low-density cloud of neutral atoms has hard, short-range collisions, with impact parameters on the order of the atom size. Gravitational and Coulomb forces are long-range with a wide variation in possible impact parameters. Individual collisions often result in only slight changes to particle trajectories, and collision effects are generally dominated by these small-angle changing collisions, as opposed to the much less frequent short-range large-angle collisions. The Boltzmann equation is very similar for both the atomic and Coulomb problem and many of the same assumptions apply, but the main difference is the form of the collision operator. Luiten *et al* found numerical solutions to the Boltzmann equation in the neutral atom trap and the atom distribution was well approximated by the truncated Boltmann distribution [86]. The original solutions for the gravitational case were found decades ago by Michie [84] and King [85] and found to show good agreement with observations from star clusters [85].

We also note similar laboratory experiments on the evaporation of charged particles from one-component plasmas in Penning traps. The difference in these experiments is that the trap for the charged particles comes from an external set of electrodes, and the potential can either be held fixed or controllably changed. Most recently, forced evaporation out of these traps has been used to create cold samples of antiprotons [87], and highly charged ions [88].

While the form of the high-energy tail of the electron thermal distribution is an interesting problem and a necessary consideration in theoretical models, we have not been able to devise an experiment capable of distinguishing a Michie-King from a Maxwell-Boltzmann distribution in our system.

2.3.2 Temperature Measurements

Experimental measurements of the electron temperature have been limited. Roberts et al [24] used slight voltage pulses to dump only the high-energy tail of the electron distribution from the plasma. The percentage of electrons dumped was used to infer the temperature. An important finding was that the electron temperature at 10-15 μs after ionization was to first order independent of the initial temperatures, which shows both the strong effect of adiabatic cooling from high initial temperatures and the strong effect of TBR heating from low initial temperatures. Despite the fact that this measurement probes the high-energy tail of the distribution, the experimental uncertainty was too large to distinguish the shape of the distribution.

Temperature dependent plasma processes provide an alternative route to mea-

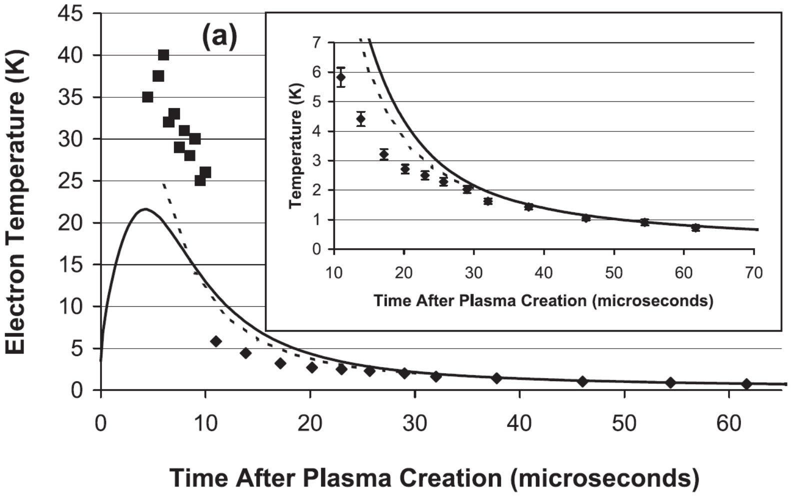

Figure 2.6: Summary of electron temperature measurements. Squares are from the spilling measurement [24] with $E_e/k_b = 10$ K and diamonds are from the TBR measurement [21] with $E_e/k_b = 3$ K. The dashed and solid lines are simulation results for $E_e/k_b = 66$ K and 3 K; note the similar values at times $> 10\ \mu$s. The inset highlights the TBR measurement results. Reprinted from [21].

suring temperature. Fletcher et al [21] used a measurement of the TBR rate to infer the temperature. The TBR process is particularly nice since the rate scales strongly with temperature, $R_{TBR} \propto n_e^2 T_e^{-9/2}$, so that moderate uncertainty in R_{TBR} will not have a significant effect on T_e. This measurement showed the continued decrease of T_e between 20 and 60 μs to values approaching 1 K. Figure 2.6 summarizes both temperature measurements.

2.3.3 Electron Fraction

We now seek finite temperature corrections to our zero-temperature solution for the electron spatial distribution and electron fraction. As in the zero-temperature case, we consider a fixed point in time and stationary ion density ρ_i. For a given electron distribution function f_e, the electron density ρ_e and electric potential ϕ are

$$\rho_e(\mathbf{r}) = en_e(\mathbf{r}) = \int f_e(\mathbf{r}, \mathbf{v})\mathrm{d}\mathbf{v} \tag{2.4}$$

$$\phi(\mathbf{r}) = \phi_c(\mathbf{r}) - E_{ext}z, \quad \nabla^2\phi_c(\mathbf{r}) = (\rho_e - \rho_i)/\epsilon_0 \tag{2.5}$$

with f_e taking the MK form

$$f_e(\mathbf{r}, \mathbf{v}) \propto (e^{-(mv^2/2 - e\phi(\mathbf{r}) + e\phi_0)/k_bT_e} - 1) \tag{2.6}$$

where ϕ_0 is the potential at the saddle point, and f_e is normalized to N_e electrons. A numerical algorithm that iteratively solves Eqs. 2.4 and 2.5 results in a self-consistent solution for the complete potential and density with input values of N_e and T_e. For each T_e, there will be a range of N_e that give reasonable solutions, the difference being the relative depth of the potential well. This approach has been used before in simulations of UCPs [1, 34, 35, 80] but without an applied field.

The symmetric problem has been solved in detail for the case of a MK distribution by Vrinceau [80]. As stated before, plasma expansion without the electric field can be consistent with no electron loss. We assume ideal expansion and assume a constant number of electrons $N_e/N_i = 1 - \delta_{\text{prompt}}$, where $\delta_{\text{prompt}} \approx 0.05$ is the fraction lost in the prompt peak. We iteratively solve for the plasma potential during expansion and find the potential depth decreases more slowly than the temperature such that $\eta = \phi(r = 0)/k_bT_e$ increases with time.

To start the iterative algorithm including the applied field, we use the calculated zero-temperature electron density renormalized to have slightly fewer electrons as the initial guess of the electron density. We calculate the total density and electric potential and then use the MK distribution to calculate the new electron density. Since we seek to calculate N_e, this can not be an input to the algorithm and we need a different way to normalize f_e. We choose to fix the relative well depth at $\eta = 5$ (the value is largely arbitrary, but based on our experience with neutral atom evaporation), where η is now defined as the difference between the saddle point and the potential minimum, $\eta = (\phi_0 - \text{minimum}[\phi, z = 0 \text{ to } z_{\text{saddle}}])/k_b T_e$. The density passed to the next iteration is the previous density with only a small fraction of the newly calculated density mixed in. The farther away the density is from the correct self-consistent solution, the smaller the mixing fraction needs to be to prevent divergence of the algorithm. (In fact, we were unable to successfully converge this algorithm before solving the zero-temperature problem, which gives an initial guess already very close to the correct density.)

Figure 2.7 shows an example solution of the plasma potential and density. The potential depth is set by the input values of T_e and η. The electron density shows the thermal smoothing of the hard edges from the zero temperature solution. A useful check on our result is to note the agreement of the total plasma density at the plasma center, where the external field is sufficiently screened, to the analytic solution from the symmetric problem [1]:

$$\rho_i - \rho_e = \frac{3 k_b T_e \epsilon_0}{e \sigma^2} \tag{2.7}$$

Figure 2.8 shows a comparison of the self-consistent solution to the measured electron fraction and the fraction from the zero-temperature algorithm. The zero-temperature theory is fit to the data to get values of v_0 and N_i. These numbers

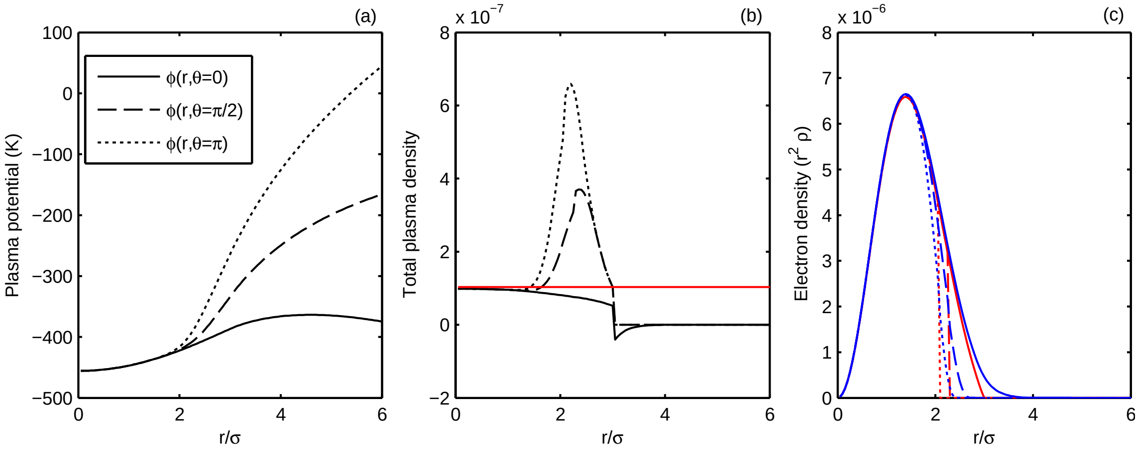

Figure 2.7: Self-consistent solution of Poisson's equation. (a) The electric potential of the plasma. (b) The total plasma density $\rho_i - \rho_e$. The red line indicates the analytic solution of symmetric problem. (c) The electron density (blue) compared to the zero-temperature electron density (red) for the same values of N_i, σ and E_{ext}. In (a)-(c), the solid, dashed and dotted lines refer to the solution at angles $\theta = 0$, $\theta = \pi/2$ and $\theta = \pi$ respectively. Initial plasma parameters are $E_e = 100$ K, $N_i = 0.23 \times 10^6$, $E_{ext} = 50$ mV/cm, $\sigma_0 = 300$ μm. The plots were made at $t = 7.5$ μs after ionization when $T_e = 18$ K. We assumed $\eta = 5$ and solved for $N_e = N_e(T = 0) - 0.043 = 0.835$.

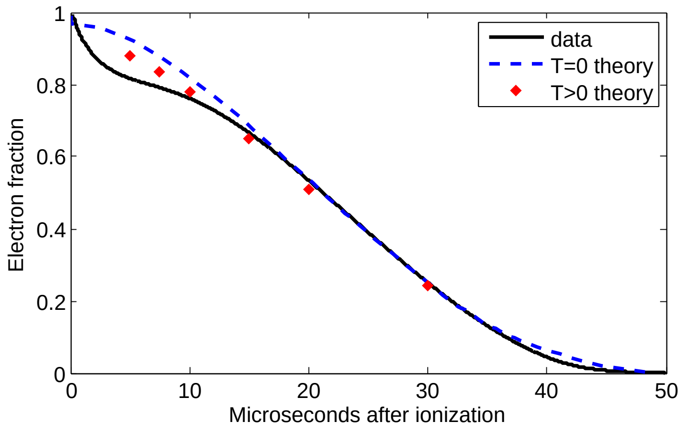

Figure 2.8: Electron fraction theory comparison. Comparison of finite temperature electron fraction to zero temperature theory and data. The data was fit to the zero temperature solution. Initial plasma parameters are the same as in Fig. 2.7.

are input to the finite temperature self-consistent algorithm and we find solutions for N_e at six points in time. There is clearly only a small deviation from the zero-temperature solution, especially at later time when T_e is lower. At 5 - 10 μs, we can input the measured values of N_e/N_i to the self-consistent algorithm and calculate the potential depth η (instead of inputing η and calculating N_e/N_i). For the example in Fig. 2.8 we get $\eta = 10 - 12$, but there are uncertainties in the determination of the initial charge imbalance and other plasma parameters that have a significant impact on these numbers.

While we believe both the zero-temperature and finite-temperature models to be good approximations, especially considering the excellent agreement with our electron current signals, some assumptions may not be valid. First of all, the MK distribution was derived only for the case of a spherically-symmetric Gaussian density distribution, rather than the asymmetric distributions we use. The singular spatial position of the saddle point may make the quasi-equilibrium assumption less accurate, as high-energy electrons stuck in orbits that do not cross the region of the saddle point are allowed to stay in the trap. We also have assumed that the mean free path, λ_{mfp}, for an electron is larger than the system size, so that a global equilibrium is established on the electron collision time-scale. While this is true at plasma creation, λ_{mfp}/σ decreases with expansion and eventually drops below 1. This last condition is more strongly violated for high density UCPs.

2.4 Pulsed Electron Emission

The above description assumed that the external electric field was constant throughout the plasma expansion. But both models will be accurate for varying electric fields, as long as the variation is slow compared to the electron collision time and the applied field is not large enough to significantly disrupt the ion expansion. We have performed experiments where we apply a short voltage pulse to the plasma that dumps a fraction of the electrons, causing an interruption in the electron signal. We discuss this measurement in the context of our new understanding of the electron distribution. In Chapter 3 we will use it in measurements of plasma oscillations.

We apply a short voltage pulse to the plasma at a variable time after ionization. We use voltage pulses of 0.5-2 μs length, chosen to be longer than the electron collision time, which remains less than 1 μs for most of the plasma expansion. The electrons then maintain a quasi-equilibrium during the pulse, but the pulse is still short compared to the ion expansion. Some examples of the electron emission signal

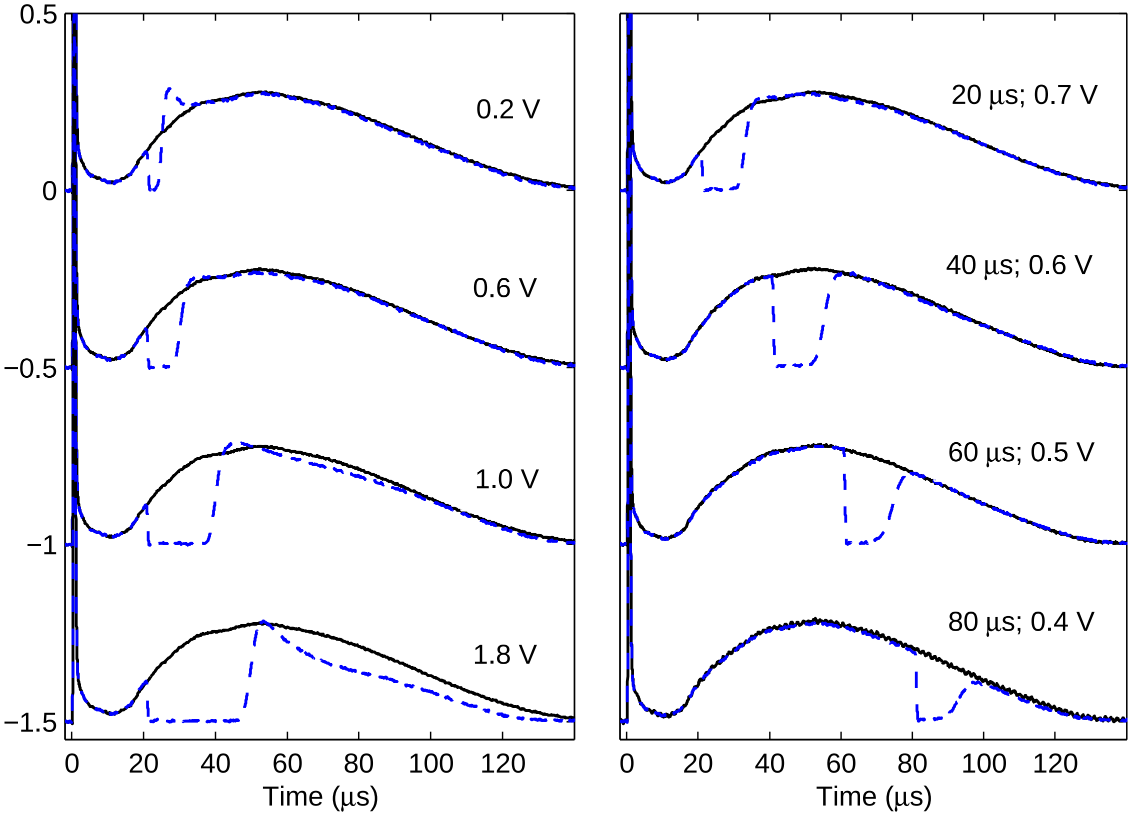

Figure 2.9: Pulsed electron emission. (Left) Electron signals with a voltage pulse of 1 μs length applied at 20 μs with varying voltages. Solid black lines are electron signals without a pulse and dashed blue lines are signals with a pulse. (Right) Electron signals with pulses applied at varying times. Here we show voltage values where the end of the electron signal nearly perfectly matches the unperturbed signal.

with pulsed emission are shown in Fig. 2.9. The polarity of the voltage pulse is opposite to that of the bias field, so the pulse dumps electrons away from the detector. The effect of the pulse is to suddenly reduce the number of electrons in the plasma; electron emission ceases for 5-20 μs and then quickly returns to follow the original curve.

Before the voltage pulse, the plasma is freely expanding, where we assume a Gaussian ion distribution and an asymmetric electron distribution. After the pulse, the remaining electrons will be concentrated mostly at the center of the ion distribution. The dc electric field will still polarize the plasma, but there are not enough electrons to stretch the electron distribution to the edge of the ions. We can calculate the new electron distribution using the same algorithm used in Sec. 2.2 but fixing the value of the electron fraction N_e/N_i. The result is shown in Fig. 2.10. The cessation of electron emission is now easily understood as the electrons are held in a deep well such that no electrons reach the edge of the ion cloud. As the plasma continues to expand, the well depth decreases and the electron distribution slowly becomes less symmetric until it again reaches the edge of the ion distribution and electron emission returns.

The drop in N_e must have some effect on the ion expansion, as the ions outside the volume of the electron cloud are free to move in response to both the external field and their own interactions without electron screening. For larger electron dumps, the density of free ions is large enough that a significant Coulomb explosion occurs and disrupts the following neutral plasma expansion. The electron emission signal following a pulsed emission is a good indicator of the magnitude of this effect. Since the rate of electron emission is directly related to the size and shape of the ion cloud, an electron emission signal very similar to the unperturbed expansion should indicate a minimal change in plasma expansion, and as shown in Fig. 2.9 we can in some cases get remarkably good agreement in the late-time emission signals. But for large voltage pulses, the returning electron signal can become significantly distorted. Generally the pulsed emission only works well at times later than 20 μs

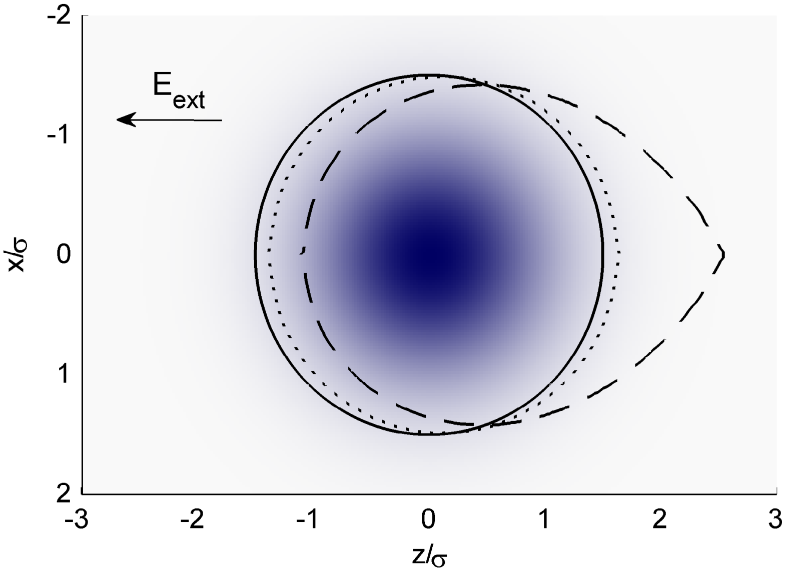

Figure 2.10: Electron distribution comparison. Electron distributions along the axis of the applied field with $N_e/N_i = 0.47$. The shaded region represents the Gaussian ion distribution. Cold electron distributions match n_i inside the boundary lines and drop sharply to zero outside. The dashed line is the asymmetric boundary during unperturbed plasma expansion and the dotted line is the electron boundary after a pulsed dump of electrons. The solid line shows the boundary for a perfectly symmetric electron distribution with the same fraction of electrons.

after ionization for a typical plasma of $N_i = 10^6$. At earlier times we cannot dump a sizable number of electrons without the freed ions modifying the expansion.

These experiments further demonstrate the quality of the zero-temperature approximation in describing the electron emission. They also demonstrate that we can control the charge imbalance of the plasma and also the shape of the spatial distribution without significantly altering expansion. The return of the electron signal after a pulsed dump may also provide a route to measuring the thermal distribution. For zero-temperature electrons, the electron signal should return instantaneously to non-zero emission once the density decreases far enough for the external field to force emission. The smooth return that we observe must contain information about the electron thermal distribution, particularly the high-energy tail since those are the first electrons to escape. But any measurement will require careful examination of the pulsed emission's impact on ion expansion.

Chapter 3

Collective Modes

Collective oscillations are central to the study of plasmas as they embody the rich physics unique to the plasma state and provide diagnostics of plasma density and temperature. The inhomogeneous density, expansion, changing neutrality and changing temperature make UCPs a novel system for the study of collective phenomena. Previous experiments on UCPs have observed plasma oscillations [22], Tonks-Dattner resonances [39], a high frequency electron drift instability [26] and ion acoustic waves [16, 17]. Studying ion waves is a promising route to testing the effects of strong coupling in UCPs. While the electronic component never reaches strong coupling ($\Gamma_e = 0.1 - 0.2$), a detailed understanding of electron modes has been difficult due to the complexity of the time-varying electron distribution.

Plasma oscillations, the simplest collective mode, can be used as a diagnostic of the time-varying density, but only if the relationship between the resonant frequency and inhomogeneous density is known. The ions in a UCP have a Gaussian density, and early studies assumed an equivalent electron density [22, 89]. A recent study has included the effect of the decreasing neutrality of the plasma as electrons are lost [90] and found the resonant frequency to increase for plasmas with fewer electrons, as the electrons are concentrated near the center of the ion distribution. All theories assumed a spherically symmetric electron spatial distribution, but we have found there to be a significant asymmetry in our experiments (Chapter 2) [81] and the effect of this on electron oscillations has not been addressed.

In this chapter, we excite and detect plasma oscillations of an UCP taking into account the changing density, neutrality and symmetry of the electron distribution [91]. We use a combination of constant and pulsed electric fields to control the plasma neutrality and find the variation of the resonant frequency with neutrality agrees well with the predictions of [90]. In addition, we have developed a new diagnostic for UCPs where we directly detect oscillations through the current induced on a nearby electrode. Electronic detection avoids heating and evaporation dynamics associated with previous measurements based on enhanced electron emission, and we can use it in experiments where charged particle detection is not possible. We also use the new diagnostic to observe hybrid oscillations of the electrons and discuss the possibility of measuring damping.

3.1 RF Mode Detection

Information about the electrons in UCPs has thus far predominantly been obtained by monitoring the loss rate on a charged particle detector as described in Sec. 1.4. This method of electron detection has succeeded in observing plasma oscillations [22, 39], but only indirectly by applying a constant driving field, allowing the field to resonantly heat the electrons and observing an enhancement in the loss rate from the plasma. Figure 3.1(a) shows electron signals with and without a constant rf field applied. The extra peaks in the electron signal with rf field correspond to times when the plasma density (decreasing with expansion) reaches a value that is resonant with the driving field. But the timing of the peaks are subject to the dynamics involved with heating the electrons and their subsequent evaporation.

We present a new approach to studying electron resonances in ultracold plasmas by directly measuring changes in the rf field. Measurements of rf power absorption are commonplace in low density laboratory plasmas. Most analogous to our system are measurements of zero-temperature oscillations done on nonneutral plasmas trapped in Penning traps [92–95]. Similar work has used these modes as a diagnostic of electron and positron plasmas as a step in the production of antihydrogen [96–99]. These plasmas are typically of similar size and density to our neutral plasmas, but our rapidly expanding plasmas are untrapped so the measurements must be made during the fast time evolution of the plasma density. Our resonances last only a few μs, about 100 times shorter than the averaging times used for nonneutral plasmas, making ours a technically more challenging task.

The modes are detected by applying a weak, continuous rf drive at frequency ω_{rf} to the grid located above the plasma and monitoring the amplitude and phase changes of the voltage coupled to the symmetric grid below the plasma, $V_b(t) = A(t) sin(\omega_{\mathrm{rf}} t + \phi(t))$, as sketched in Fig. 3.2. We use a standard homodyne measurement to measure the changes in V_b caused by the plasma. The voltage is amplified and mixed down to dc; we control the phase of the local oscillator (LO) and take measurements when the phase difference between the rf and LO signals at the mixer is 0 or $\pi/2$. The output of the mixer to first order is the multiplication of the

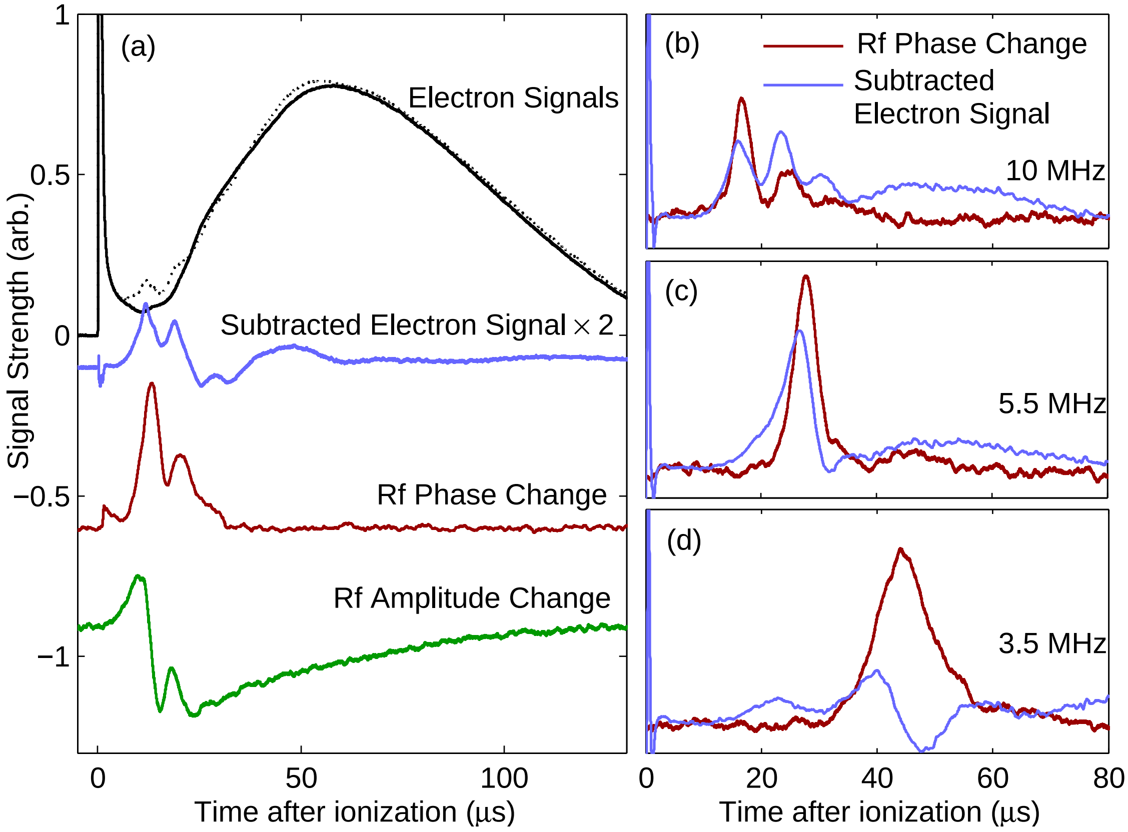

Figure 3.1: Comparison of rf signals to electron signals. (a) The subtracted electron signal (blue line) is the difference of the recorded electrons signals with (dotted black line) and without (sold black line) a $f = \omega_{\mathrm{rf}}/2\pi = 14$ MHz rf field applied. The rf signals have been rescaled by the same arbitrary factor, and are offset for clarity. (b)-(d) Rf phase change compared to subtracted electron signal for three different frequencies.

received and LO signals

$$M_{\mathrm{out}} = A(t)sin(\omega_{\mathrm{rf}}t + \phi(t))Lsin(\omega_{\mathrm{rf}}t + \theta) \tag{3.1}$$

where L is the LO amplitude and θ is the controlled phase. In the absence of a plasma, V_b is constant in time and is due to capacitive coupling between the electrodes, so M_{out} is a constant dc voltage (higher frequencies are filtered out). When a plasma is present and driven near a resonant frequency, the oscillation of the plasma induces a current on the bottom grid that interferes with the background signal. The signal from the plasma is much smaller than the background at all frequencies that we measure, so we observe only small changes in the recorded dc voltages as the plasma density quickly scans through resonance with the driving field. We can approximate $A(t) = A_0 + \delta A(t)$ and $\phi(t) = 0 + \delta\phi(t)$. To first order in δA and $\delta\phi$ the mixer output is

$$M_{\mathrm{out}} = \frac{A_0 L}{2}(1 + \frac{\delta A(t)}{A_0}) \quad \text{if } \theta = 0 \tag{3.2}$$

$$M_{\mathrm{out}} = \frac{A_0 L}{2}\delta\phi(t) \quad \text{if } \theta = \pi/2 \tag{3.3}$$

The measured signals are directly related to the amplitude and phase change of V_b and examples are shown in Fig. 3.1. Only the relative change in the signals due to the plasma is shown.

For frequencies $f < 20$ MHz, we use a low-noise high-bandwidth transimpednace amplifier (Femto model HCA-10M-100K-C or HCA-100M-50K-C) to amplify the rf signal. But for $f > 20$ MHz, the 30 pF shunt capacitance of the vacuum feedthrough (a HV feedthrough that is not impedance matched), which connects

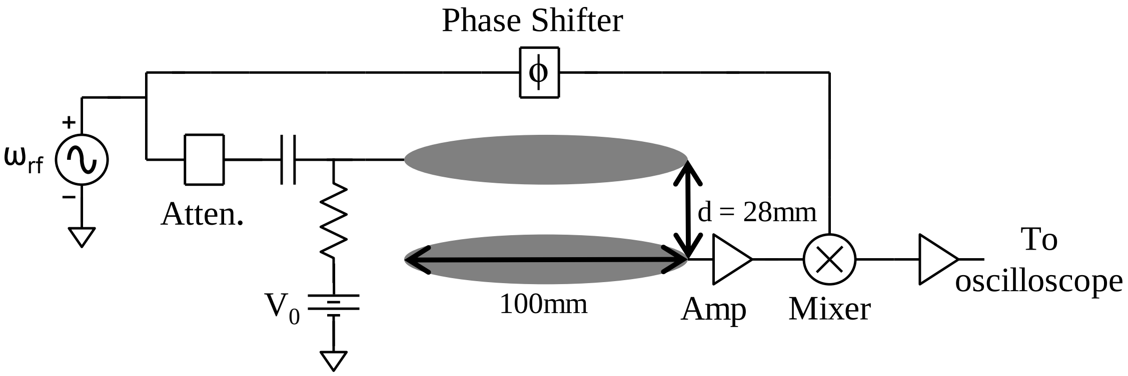

Figure 3.2: Schematic for homodyne detection of plasma oscillations.

the grid to the amplifier, degrades the performance, so a voltage amplifier is used instead. The maximum current induced by the plasma is on the order of a few nA. After mixing down to DC, the signal is filtered and amplified again. All measurements are done with $\geq$ 200 kHz bandwidth, sufficiently large to capture the fast changes in the rf signals. Due to this large bandwidth and small currents, the signal-to-noise ratio on a signal experimental shot is often less than 1, so all rf curves shown in this chapter are an average of at least 150 shots (generally more at higher frequencies where the amplifier noise is worse).

The shapes of the signals can be understood by modeling the plasma as a series RLC oscillator in close analogy with [92]. First, consider a single electron between two infinite capacitor plates. The electron charge will induce a charge on each plate that is proportional to the fractional distance of the electron to the plate. If the electron is moving with a velocity perpendicular to the plates (z direction), the current induced is simply

$$i = e\dot{z}/d \tag{3.4}$$

where d is the distance between the plates. If we now imagine the electron to be oscillating in a harmonic potential at the center, the equation of motion for the electron is

$$m_e \ddot{z} + m_e \omega^2 z = eV/d \tag{3.5}$$

where V is the driving voltage across the capacitor and ω is the oscillation frequency. Using Eq. 3.4 we can rewrite the equation of motion as the current in a driven LC circuit with $L_1 = md^2/e^2$ and $C_1 = 1/L_1\omega^2$. For a system of N_e electrons in the same harmonic trap, the induced current is proportional to the velocity of the center of mass of the electrons [92], and the same equivalent circuit representation is satisfied with $L_N = L_1/N_e$ and $C_N = 1/L_N\omega^2$. We add a resistance, R_N, to this model to account for damping, but its value is left as a free parameter.

This circuit model describes plasma oscillations in our UCP, where we have approximated the confining potential of the Gaussian ions as being perfectly harmonic with a (time-varying) trap frequency set equal to the resonant frequencies expected from theory [90]. A better model would require detailed knowledge of the oscillating dipole moment of the plasma from the resonance theory. The dependence of L on N_e is an important component of the model since N_e is decreasing during the expansion of our plasma as electrons evaporate.

An equivalent circuit including this model for the plasma and the capacitance of the grids and vacuum chamber is shown in Fig. 3.3. We solve this model to find the voltage at the amplifier input, $V_b(t)$, and find good agreement with our observed signals, considering only a single resonance. We present only this qualitative picture

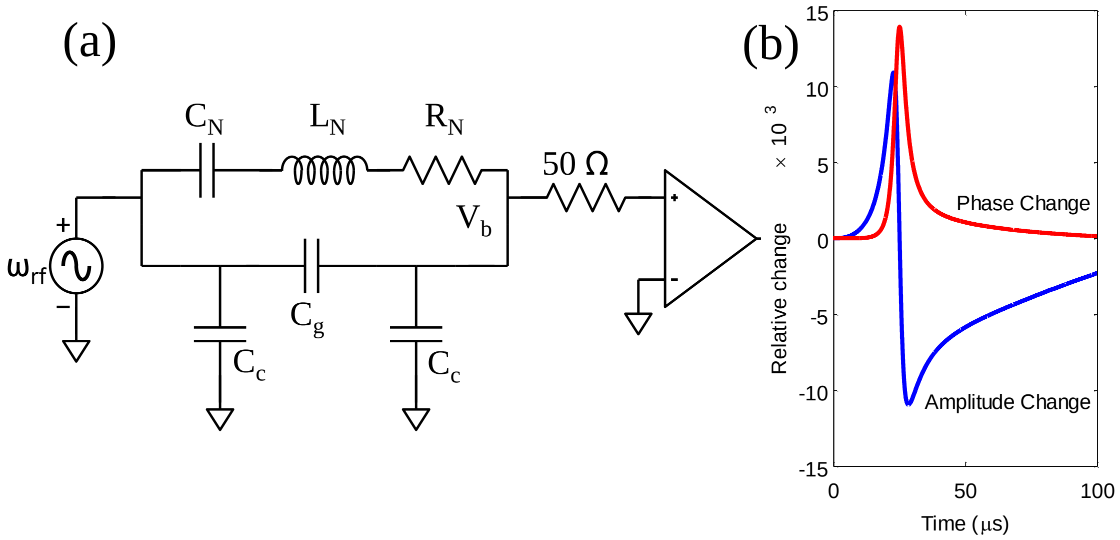

Figure 3.3: Equivalent circuit model for electronic mode detection. (a) Equivalent circuit schematic treating the plasma as an RLC oscillator. C_g is the capacitance between top and bottom grids and C_c the capacitance between each grid and the grounded vacuum chamber. (b) Relative amplitude and phase change of the voltage V_b calculated from the model in (a) with typical plasma parameters and a resonance at 25 μs. The phase change is relative to $\pi/2$.

here to show that the resonance time is associated with a peak in the phase change signal, and thus we will focus on this signal in the remainder of the analysis.

Figure 3.1 shows the comparison of the rf measurements with the enhanced electron emission for a 14 MHz drive. The resonance times in the two methods agree to within 1 μs in most cases, after correcting for a delay due to finite bandwidth, which provides support for previous results published using electron emission. There is disagreement at low driving frequency ($<$ 6 MHz), where the electron signal becomes less reliable. The electron signal measures the rate of evaporation caused by excess heating, but we should not expect a linear relationship between energy absorption and electron emission. As the heating begins and some extra electrons are lost, the plasma potential well deepens, so a greater input energy is needed to subsequently maintain the same electron flux. This effect is most evident at low frequencies as the plasma response becomes much broader in time. By contrast, the rf signal is measuring an induced current that is directly proportional to the amplitude of electron oscillations. The rf measurement is more direct and can also be used in experiments where the electron detection is complicated or impossible (e.g. when magnetic fields are applied transverse to the grid axis).

For large plasmas, we routinely see multiple peaks in the electron emission signal, previously identified as Tonks-Dattner resonances [39], but we typically see only the first two in the rf signal. For larger driving amplitude we can resolve a third peak in the rf signal, but it is a factor of 10 or more smaller in amplitude than the first peak. We anticipate that a higher signal-to-noise measurement would allow us to see all of the modes. We do not have a model to explain the observed amplitude of the higher modes or why more are visible in the electron emission. We focus mainly on the zero-temperature plasma resonance, which is the earliest-time feature in both the electron emission and rf signals.

3.2 Zero Temperature Plasma Oscillation

3.2.1 Theory

To understand the observed resonance time, we must consider the full picture of the spatial distribution of electrons. Optical measurements of the plasma ions have conclusively shown the ion spatial distribution, n_i, to maintain a Gaussian density throughout the plasma expansion, given by Eq. 1.5. At the center of the plasma, the electron density must be nearly equal to the ion density, but electron loss ensures deviations at the plasma edge.

Plasma oscillations induced by a weak external drive are modeled by a zero-temperature electron fluid with a small density modulation. The cold fluid equations are

$$\frac{\partial n_e}{\partial t} + \nabla \cdot (n_e \mathbf{v}) = 0 \tag{3.6}$$

$$\nabla^2 \phi = -e(n_e - n_i)/\epsilon_0 \tag{3.7}$$

$$m_e(\frac{\partial \mathbf{v}}{\partial t} + \mathbf{v} \cdot \nabla \mathbf{v}) = -e\mathbf{E} - \nu m_e \mathbf{v} \tag{3.8}$$

In these equations, $\mathbf{v}$ is the electron velocity, $\mathbf{E}$ is the total electric field, ν is a damping rate, and the electron density has a modulation induced by a driving rf field: $n_e = n_e^0 + \delta n \; exp(-i\omega_{\mathrm{rf}} t)$.

Bergeson and Spencer [89] solved the equations for a perfectly Gaussian electron density, assuming no electron loss, so that $n_e^0 = n_i$. They found only a single quasi-mode with a maximum energy absorption at a frequency $\omega = 0.24\omega_{p0}$, where $\omega_{p0} = \sqrt{e^2 n_{e0}/m_e \epsilon_0}$ and n_{e0} is the central plasma density. But even early in the plasma lifetime the charge imbalance may be non-negligible, owing to the prompt loss of electrons at plasma creation (Fig. 3.1).

Lyubonko et. al. [90] allowed for electron loss by treating the electron density as a truncated Gaussian, $n_e^0 = n_i \Theta(R - r)$, with the truncation radius R set by the number of electrons

$$N_e = 4\pi \int_0^R n_e^0 r^2 dr \tag{3.9}$$

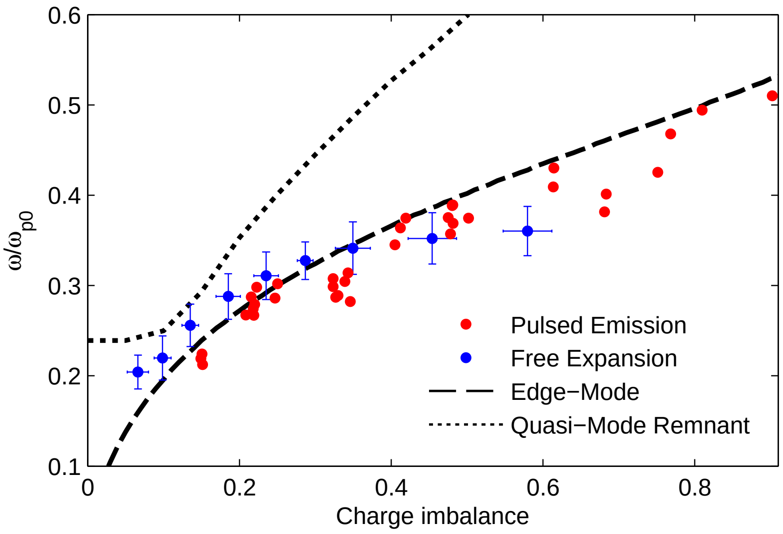

Figure 3.4: Edge-mode theory compared to free expansion and pulsed emission data. The edge-mode and quasi-mode remnant curves are from [90]. Blue points with error bars are the average of many free expansion measurements. Red points are individual measurements after pulsed electron emission. An individual measurement is an rf phase signal constructed from the average of 150-400 shots. Results are the combination of many experimental runs all with $E_e/k_b = 100$ K and $6 \times 10^5 < N_i < 10^6$.

For this electron density, the mode frequencies will depend on the normalized charge imbalance

$$\delta = (N_i - N_e)/N_i \tag{3.10}$$

where N_i and N_e are the number of ions and electrons. For plasmas with any significant charge imbalance ($\delta \geq 5\%$), they found a mode where the majority of energy was absorbed near the sharp edge of n_e^0. The relative frequency of the edge-mode resonance, $\omega_{rel} = \omega/\omega_{p0}$, was found to increase with the charge imbalance as shown in Fig. 3.4. For large δ, the frequency approaches $\omega_{rel} = 1/\sqrt{3}$, the plasma frequency of a uniformly charged sphere.

These theories have assumed a perfect spherical symmetry, but this is in contrast to the asymmetry we have found in n_e^0 in our typical experiments. The difference between our calculated electron distribution and the symmetric case for the same charge imbalance is shown in Fig. 2.10.

3.2.2 Measurement with Free Expansion Signal

We perform two types of experiments to test the edge-mode prediction. First, we record the resonance times from the rf signal, as in Fig. 3.1, for different ω_{rf}. For smaller ω_{rf}, the resonances are observed later in time, corresponding to a lower density. But due to the continuous electron loss, later time also corresponds to larger charge imbalance, which should increase the relative resonant frequency. Examples of rf signals are shown in Fig. 3.1 compared to the electron signal for different ω_{rf}.

We fit a Gaussian to the first peak of the rf phase change signals to get the resonance time (we do not expect the resonance to be Gaussian in time; this is just an easy way to find the peak). We independently measure the plasma expansion velocity using the ion current signal and the ion number using the electron current signal as in Sec. 2.2.2. This allows us to calculate ω_{p0} and $\omega_{rel} = \omega_{\mathrm{rf}}/\omega_{p0}$. The charge imbalance is easily calculated by integrating the electron signals. Only a small 10-15 mV/cm electric field is needed to direct all escaping electrons to our detector in a free expansion experiment (for higher fields there is no increase in the integrated current on the detector). The fraction of the integrated current that arrives before the resonance time gives the charge imbalance δ. The results are shown in Fig. 3.4.

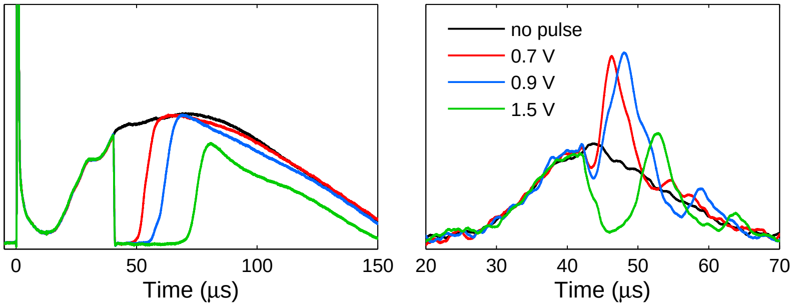

Figure 3.5: Rf signals during pulsed electron emission. Electron signals (left) and rf phase change signals (right) with a voltage pulse of 1 μs length and varying amplitude applied at 40 μs. The applied frequency is $f = 4$ MHz. The vertical axes are linear scales with arbitrary units.

3.2.3 Measurement with Pulsed Electron Emission

In the second experiment, we use the method of pulsed electron emission (Sec. 2.4) to have independent control over the charge imbalance and to attempt to create a plasma where n_e^0 is closer to the symmetric distribution used in the edge-mode theory. Fig. 3.5 shows examples of electron and rf signals with both a continuous rf drive and a pulsed electron emission.

For a given voltage pulse height and time, we adjust the rf frequency and look at the rf signal during the dead time of the electron emission. When we are near a resonance, a clear sharp peak is observed during the dead time that we identify as the edge mode resonance. We find the time of resonance and calculate ω_{rel} assuming an uninterrupted Gaussian expansion. Figure 3.5 shows a comparison of resonance measurements for different strengths of voltage pulse. Changing the strength of the voltage pulse dumps more electrons, increasing δ, but leaves all other parameters unchanged. We see that this direct change in charge imbalance increases the time of resonance, which corresponds to an increase in ω_{rel} as predicted. We can only increase the voltage pulse a small amount before the size of the electron dump becomes too much of a perturbation to the expansion. To get to higher charge imbalance, we wait until later time in the expansion, letting the plasma naturally lose more charge, before applying the pulse. At later time we find the resonances at lower frequency and in this way can map out a wide range of charge imbalance (Fig. 3.4).

The voltage pulse is applied to the top grid through the dc connection in Fig. 3.2. In the absence of a plasma, there is a small spike in the recorded rf signals at the time of the voltage pulse for all frequencies. We have subtracted this background signal from the rf phase signals recorded with the plasma.

During pulsed emission, we pulse the electrons away from the detector but still collect all electrons at other times. The charge imbalance is found by comparing the integrated current after the time of resonance to the full integrated current in the unperturbed experiment.

In addition to the charge imbalance, we also expect the pulsed emission to affect the shape of the electron distribution, as in Fig. 2.10. Figure 3.6 shows the result of a frequency sweep at fixed pulsed emission parameters and the calculated values of ω_{rel}. We find that higher frequencies, where the peak comes soon after the pulsed emission, give the closest agreement to the edge-mode prediction. Since δ does not change during the time when electron current is zero, the change in ω_{rel} is unexpected. We expect n_e^0 to be most symmetric immediately after the pulse and then gradually becomes less symmetric, so the observed change in resonance may

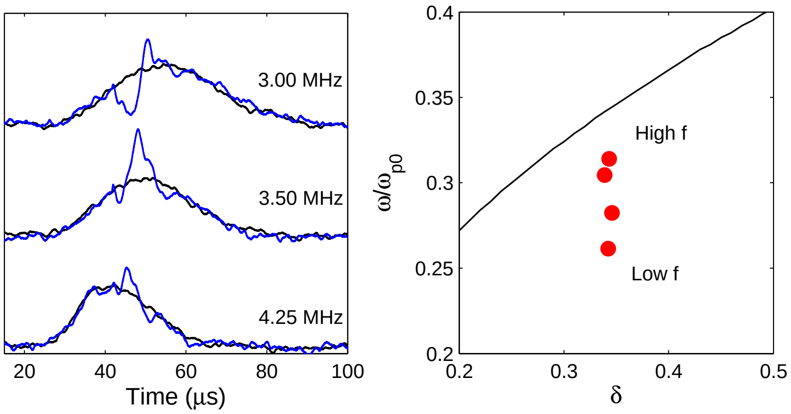

Figure 3.6: Rf sweep during pulsed emission. (Left) Rf signals with (blue) and without (black) a 0.7 V voltage pulse at 40μs for the same plasma parameters as in Fig. 3.5. (Right) The relative frequency at time of maximum in rf signal (red points) compared to edge mode theory (black).

be a measure of this effect, or it may instead be some unwanted effect of the pulsed emission on expansion which becomes more pronounced at later times. Similar frequency sweeps with different parameters show the same trend of decreasing ω_{rel} with increasing delay after the pulsed emission.

The data in Fig. 3.4 show the results of similar frequency sweeps for pulsed emission parameters that create different values of δ. We only plot points where the observed peak comes within 7 μs of the end of the voltage pulse.

It is clear from Fig. 3.4 that the free expansion and pulsed experiments agree reasonably well with each other and support the general trend of increasing ω_{rel} with δ. Agreement in the free expansion data is worst at large δ, but these rf signals are very broad, spanning 10s of μs, which increases the uncertainty in fitting a specific resonance time. There are also significant changes to the plasma density and collision rates and significant electron loss during the response time, which may affect the magnitude of the rf signal. The pulsed emission experiments give us more direct control over δ, and we can more easily probe large values. It is unclear to us why the rf signal after a pulsed emission has such a stronger and sharper response than during the normal free expansion.

The importance of the shape of n_e^0 is also not immediately clear. During free expansion, we expect n_e^0 to be asymmetric, like the dashed line of Fig. 2.10, while after pulsed emission it should be something more symmetric. The data in Fig. 3.6 suggest that the pulsed emission measurements are sensitive to shape changes in n_e^0, yet the free expansion measurements seem to agree equally well with the perfectly symmetric theory, suggesting that the spatial distribution of charge is only of secondary importance to the integrated amount of charge. It seems surprising that the position of the electron cloud edge is not a larger factor given the finding in [90] that the large majority of energy is absorbed at this edge. It would be interesting to see how the solution of the cold plasma fluid equations changes for the asymmetric distributions of Fig. 2.10.

We also note that the theory is for a zero temperature plasma. Smoothing of the edge of the electron distribution from finite temperature will tend to increase the relative resonance frequency [90].

3.3 Tonks-Dattner Resonances

We have so far focused only on the first peak in our rf and electron signals, but for large plasmas we see multiple peaks that were previously identified as Tonks-Dattner resonances [39], electron sound waves propagating in an inhomogeneous finite-size plasma [100, 101]. The original experiments on Tonks-Dattner resonances were done in a gas discharge plasma confined in a cylindrical tube [101, 102]. The tube gave a well-defined outer boundary condition for the electron waves for which there is no obvious analogy in our rapidly expanding UCPs, so the comparison of the two systems was somewhat qualitative.

Molecular dynamics simulations [103] have also seen multiple resonances in the rf absorption in UCPs. The simulations treat the ions as a fixed continuous background and calculate the dynamics of electrons in response to a weak rf drive and an electron temperature given by $\Gamma_e = 0.2$. When the simulations are performed for spherical ion and electron distributions with uniform density, only the cold plasma resonance at $\omega = \omega_{p0}/\sqrt{3}$ is found. For a perfectly Gaussian ion distribution and equivalent electron distribution, they find only the quasi-mode predicted by cold plasma theory. The multiple resonances are only seen for a Gaussian ion density and truncated Gaussian electron density. This strengthens the analogy to the original Tonks-Dattner resonances as the boundary of the truncated electron distribution (smoothed by finite temperature) can serve as the outer boundary condition for the waves.

We can measure the values of ω_{rel} and δ for the second peak in the rf signal and for all of the peaks we observe in the subtracted electron signals. All of the peaks show a trend of increasing ω_{rel} with increasing δ, similar to the zero-temperature resonance, but we have not performed a more detailed analysis.

3.4 Upper Hybrid Oscillation

An important feature of our new diagnostic is that it allows us to probe electron properties through their resonant behavior without the need for charged particle detection. This advantage was evident in our ability to observe resonances during the dead time in electron emission following a pulsed electron dump. Charged particle detection can also become complicated or completely impossible in the presence of a magnetic field applied transverse to the axis of the electric grids. In this setup we have been able to drive and observe upper hybrid resonances of the plasma, as well as other unidentified modes, that we did not previously have the ability to detect. In fact, at the low frequency end of our data presented in Sec. 3.2, even a field of 0.5 - 1 G is enough to noticeably shift the plasma resonance to the hybrid value ($\omega_c/2\pi = 2.8$ MHz at 1 G), so we must take care to eliminate stray fields. The behavior of the hybrid resonance is clear when driving near the cyclotron frequency, but the electron distribution in the presence of a magnetic field is not well understood, making a detailed analysis challenging.

Electrostatic oscillations of a cold plasma in a uniform magnetic field are a hybrid of the normal plasma oscillation and the electron cyclotron oscillation. The upper hybrid frequencies for an infinite homogeneous plasma are [104]

$$\omega_{\pm} = \frac{\omega_h^2}{2} \pm \sqrt{\frac{\omega_h^4}{4} - \omega_p^2\omega_c^2 cos^2\,\theta} \tag{3.11}$$

where θ is the angle between the axis of the magnetic field direction and the oscillation axis (the grid axis in our system), and $\omega_h^2 = \omega_p^2 + \omega_c^2$. For oscillation perpendicular to the field, Eq. 3.11 reduces to the upper hybrid frequency ω_h. There is also a lower hybrid frequency corresponding to an oscillation of the ions perpendicular to the magnetic field, but observing this requires a high level of precision in the magnetic field angle, which we can not achieve in our current setup.

To excite the upper hybrid oscillation, we apply a magnetic field perpendicular to the grid axis using either the MOT coils or the transverse coils (Fig. 1.2). The magnetic field is turned on after the MOT is turned off but before ionization. As before, we apply a constant rf field and observe changes in the rf voltage received on the bottom grid. The phase change of the rf signal for several different driving frequencies is shown in Fig. 3.7 compared to the signals received without a magnetic field. As the driving frequency approaches the cyclotron frequency, the peak in the signal broadens and moves later in time. Below the cyclotron frequency, there is no resonance, as expected since $\omega_h > \omega_c$.

The measurements are not performed with the same rf driving power. The rf measurements require calibrating the rf power to be small enough to not heat the plasma and large enough to observe signals with sufficient signal-to-noise. With no magnetic field, we increase the rf power until enhanced emission is visible in the electron signals, but at a low enough level that the lifetime of the electron signal is

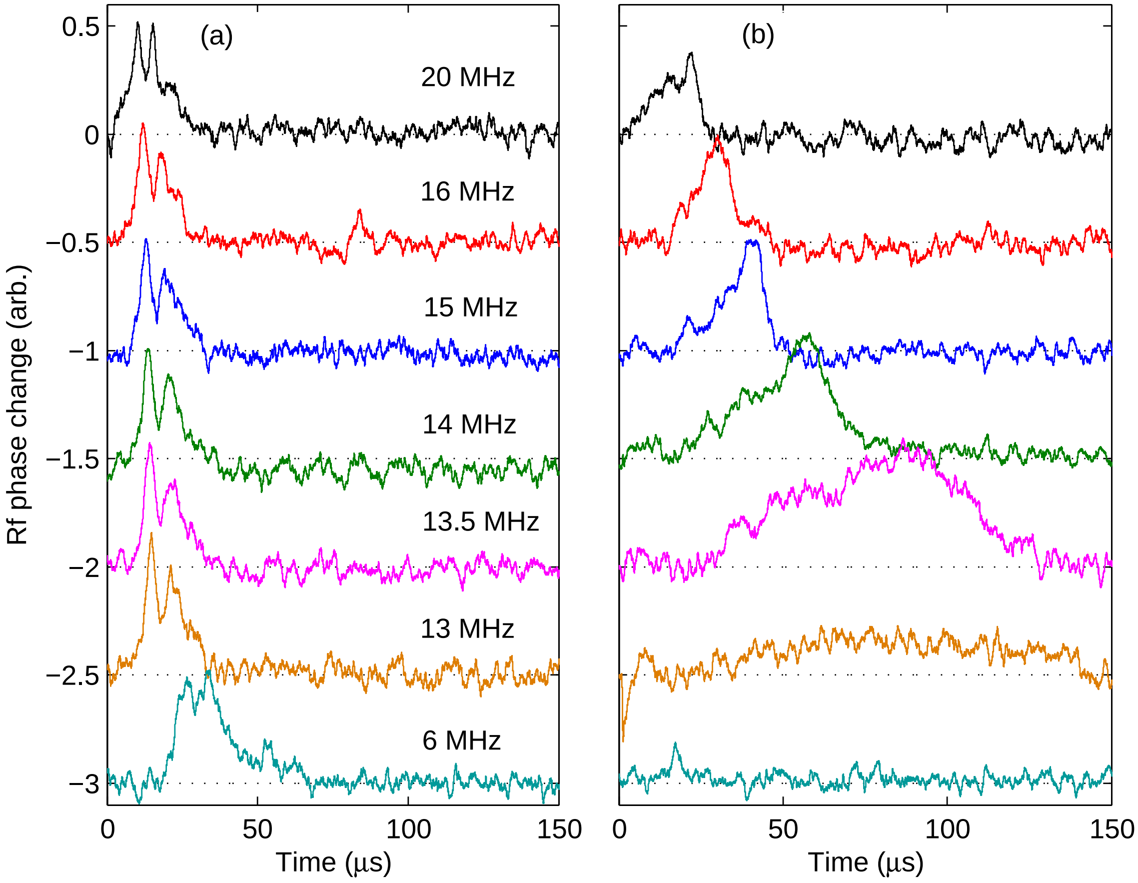

Figure 3.7: Rf signals in transverse magnetic field. Rf phase change signals at different frequencies without (a) and with (b) a $B = 5$ G field. We observe similar behavior for fields up to $B = 18$ G.

unchanged (see Fig. 3.1). With a magnetic field, we do not observe the same electron signals. We instead adjust the power until the magnitude of the rf phase change is comparable to that observed without a magnetic field (note the similar magnitude of the signals in Fig. 3.7). A small change in rf power from this value does not change the shape of the rf signals, a good indication that we are in the small-perturbation regime. In general, less power is needed to drive the hybrid resonance, and less power is needed when the resonances are found later in time, likely due to the larger plasma size, smaller damping or both.

We expect to find the resonances near the upper hybrid frequency, ω_h. For an accurate comparison, we should again consider the inhomogeneous plasma density and changing neutrality. In addition, the magnetic field slows the expansion of the plasma (although this is not a big effect at 5 G), causing the plasma to take a spheroidal shape. We do not know how the cold plasma resonance frequencies would be changed in the case of a spheroidal plasma, and we can no longer make easy measurements of the electron loss, as the transverse field prevents most electrons from reaching the detector. We approximate these considerations in the following way. We allow the plasma to expand as a spheroidal Gaussian at the reduced rate expected from the magnetic field strength (Chapter 4). We replace ω_p in Eq. 3.11 by the resonant frequency predicted from the edge mode theory and let the charge imbalance change at the same rate as it does with no magnetic field and small electric field. For a perpendicular field, the hybrid frequency is

$$\omega_h^2 = (\omega_{edge}\omega_{p0})^2 + \omega_c^2 \tag{3.12}$$

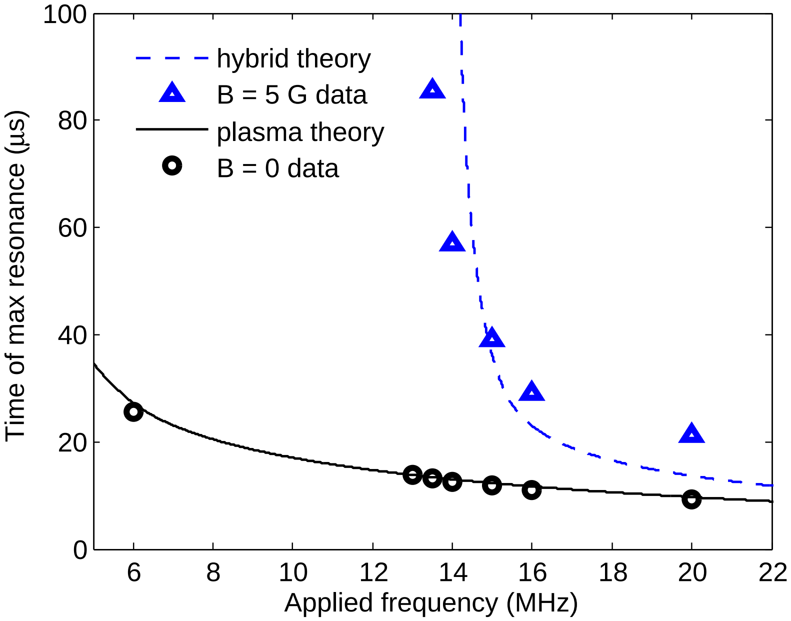

Figure 3.8: Upper hybrid oscillation. Resonance times from the curves in Fig. 3.7 compared to theory.

where ω_{edge} now represents the relative frequency from the edge-mode theory (lower curve in Fig. 3.4). The comparison of this calculation to the data is shown in Fig. 3.8. The peak times for the data are found by taking the time of maximum phase change.

We observe more modes when the angle of the magnetic field is changed. Using a combination of the longitudinal coils and the transverse coils (or MOT coils) we can apply a uniform field at an arbitrary angle to the grid axis and attempt to excite both branches of the upper hybrid oscillation, sometimes called Trivelpiece-Gould modes. For fields that are neither perfectly perpendicular or perfectly parallel to the grid axis, we do see multiple modes, one above the cyclotron frequency and one below the plasma frequency as expected. But the measured frequencies do not match well to theory. In addition, we see more modes at very low frequencies (f =

0.2 - 1 MHz) that we cannot explain.

Also note that in the presence of an electric field between the grids and a small transverse magnetic field, we observe a high frequency electron drift instability [26]. The signature of the instability is the periodic emission of electrons seen in the electron signal, with a frequency proportional to E/B. This instability is present during the measurements of upper hybrid oscillations for small magnetic fields < 10 G. For fields larger than about 10 G, electron detection is completely suppressed. An instability may still exist, although the period of periodic electron emission (proportional to B/E) will approach the plasma lifetime.

3.5 Damping

Studying mode damping should provide information on the collision properties and electron temperature in UCPs. The electronic detection gives a signal linearly proportional to the amplitude of plasma oscillations, which should provide reliable damping measurements. We have, in some regimes, been able to observe the free decay of electron oscillations after abruptly turning off the rf drive. The decay is fast, as expected from the large collision frequencies (Fig. 1.4), so a large bandwidth measurement is required, which degrades the signal-to-noise ratio. We have thus far only been able to observe the free decay of the hybrid oscillation at frequencies near the cyclotron frequency, which is apparently not as strongly damped as the plasma oscillation.

A more fruitful approach to damping may come from comparing the continuous rf signals to our equivalent circuit model, and extracting the damping term from the model. There has been considerable success measuring the temperature of nonneutral plasmas through their interaction with electrodes [92, 94, 95, 105, 106] that may serve as a guide.

Chapter 4

UCPs in External Magnetic Fields

The initial study of UCP expansion in uniform magnetic fields up to 70 G is described in the thesis of Xianli Zhang [30]. A magnetic field was generated using the longitudinal coils (Fig. 1.2) and ion projection imaging was used to measure the size of the plasma transverse to the field. The asymptotic expansion velocity transverse to the field was found to scale as $B^{-1/2}$, in agreement with an ambipolar diffusion model.

This chapter shows continuing work that extends these results. We describe the details of projection imaging in our system and take images in a transverse magnetic field to show expansion of the plasma both along and transverse to the field. We measure expansion using the ion current signal with and without a magnetic field and show evidence for a density feature at the edge of the ion distribution that has been predicted for UCPs but not previously observed. We also show evidence of reduced plasma expansion in three dimensions in the presence of a cusp field and discuss the prospects of magnetic confinement.

4.1 Ion Projection Imaging

The goal of ion projection imaging is to take advantage of the spatial resolution of the MCP to get a two-dimensional image of the plasma ion density. At a variable time after ionization, we apply a high-voltage pulse of 100 - 400 V to the top grid which immediately removes all electrons from the plasma and accelerates the ions in the direction of the MCP. The ions move through the bottom and middle grid and strike the MCP surface. The MCP in our vacuum chamber is a 40 mm diameter plate of electron multiplier channels with 12 μm channel spacing. The output of the two-stage electron multipliers strikes and illuminates a phosphor screen, creating a spatially resolved image of the charges striking the surface, and the image is captured on a ccd camera. To image the full size of the 40 mm MCP, the optical image is significantly demagnified such that 1 pixel on the ccd corresponds to a 100 μm by 100 μm area at the phosphor screen.

To properly relate these images to the ion distribution in the plasma, we must consider the ion dynamics during the time-of-flight to the detector, about 8 μs for typical accelerating voltages. The initial trajectory of the ions (at start of time-of-flight) is set by the expansion velocity of the plasma, Eq. 1.7. The ions then travel through the bottom grid and middle grid before striking the MCP front and the combination of the grids and the grounded vacuum chamber constitute a lensing system that focuses the ions onto the MCP. The ions also undergo Coulomb explosion due to their interactions with each other, the dynamics of which depend on the shape of the density distribution in the plasma.

The Coulomb explosion is the dominant effect when the voltage pulse is applied at early times, when the density is still high. At later times, Coulomb explosion is negligible; the images more closely resemble the density in the plasma, affected only by the electric lensing. For simplicity in simulating the ion optics, we consider the space-charge and electric lensing effects separately. This approximation should be reasonable since the magnification from the electric lensing is near unity, and it is sufficient to explain the basic features of our observed images.

We first consider the Coulomb explosion. Coulomb explosion of a Gaussian ion distribution has been considered before in the context of ionized cold atoms [79, 107]. The expansion is easily calculated assuming a spherically symmetric expansion of a zero-temperature charged fluid. We divide the initial distribution into N concentric shells of equal charge, distributed in space according to the initial Gaussian density, and calculate the evolution of the shell positions from the Coulomb force. The size of the Gaussian density at the start of Coulomb explosion and the initial velocity given to the shells depend on the time at which the voltage pulse is applied to the plasma. An example of the evolution of the ion density is given in Fig. 4.1(a). The Gaussian distribution is not preserved because inner shells are accelerated more strongly causing the charge to build up in a spike.

We observe this density spike in ion images taken soon after plasma creation, although the feature is muted since we are looking at the 2D projection of this density. Figure 4.1(b) shows an example of an ion image taken 5 μs after ionization for a plasma with $N_i = 7 \times 10^5$ and $\sigma_0 \approx 500$ μm. The image has a ring of higher ion density at the edge, as the Coulomb explosion predicts. A comparison of this image to the Coulomb explosion calculation is shown in Fig. 4.1(c), showing reasonable agreement. The calculation assumes no external field and a stationary center of the ion distribution, so the electric lensing will slightly modify this. We fit the calculation to the image assuming a constant ion optic magnification (discussed

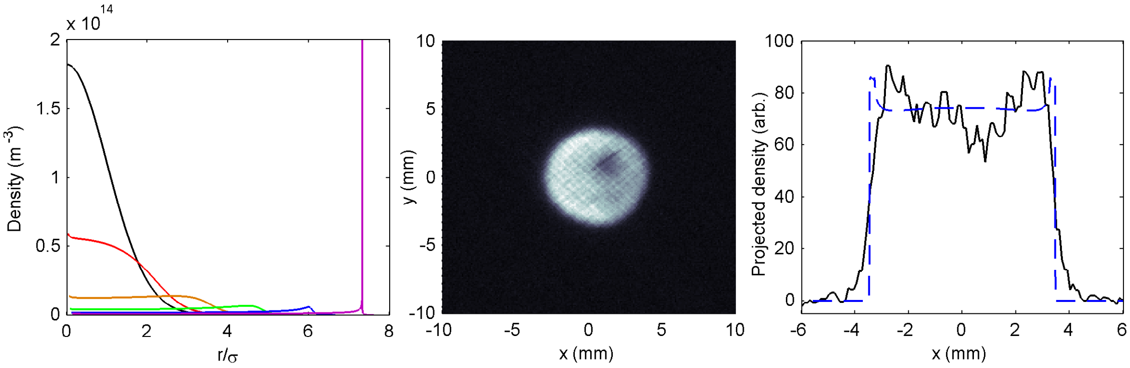

Figure 4.1: Coulomb explosion of a Gaussian ion distribution. (a) Evolution of a Gaussian ion density undergoing Coulomb expansion. Initial Gaussian has $\sigma = 625$ μm and $N_i = 7 \times 10^5$ and the curves are at 1.1 μs intervals from 0 to 5.5 μs. (b) Ion projection image taken 5 μs after ionization. (c) Comparison of a slice through image in (b) to the projection of the Coulomb expansion calculation for plasma parameters in (a) and the full 8 μs time-of-flight. The calculation is fit to the image with the electric magnification as the only fit parameter, giving a magnification of 0.53.

later).

As the imaging pulse is applied at later times in the expansion, the plasma density is lower and the Coulomb explosion effect is less. Fig. 4.2 shows ion images at varied projection times. The sharp edges and flat top features from the Coulomb explosion are most significant at $t = 0$ and not distinguishable at $t > 50$ μs.

We model the effect of electric lensing using charged particle optics software to simulate trajectories of individual ions with different starting positions through our electrode geometry. We find the ion trajectories are slightly focused onto the MCP so that the ion distribution is smaller on the MCP than in the plasma, with a magnification factor of about 0.5-1 (depending on accelerating voltages) that is relatively constant for different initial positions. There is considerable uncertainty in

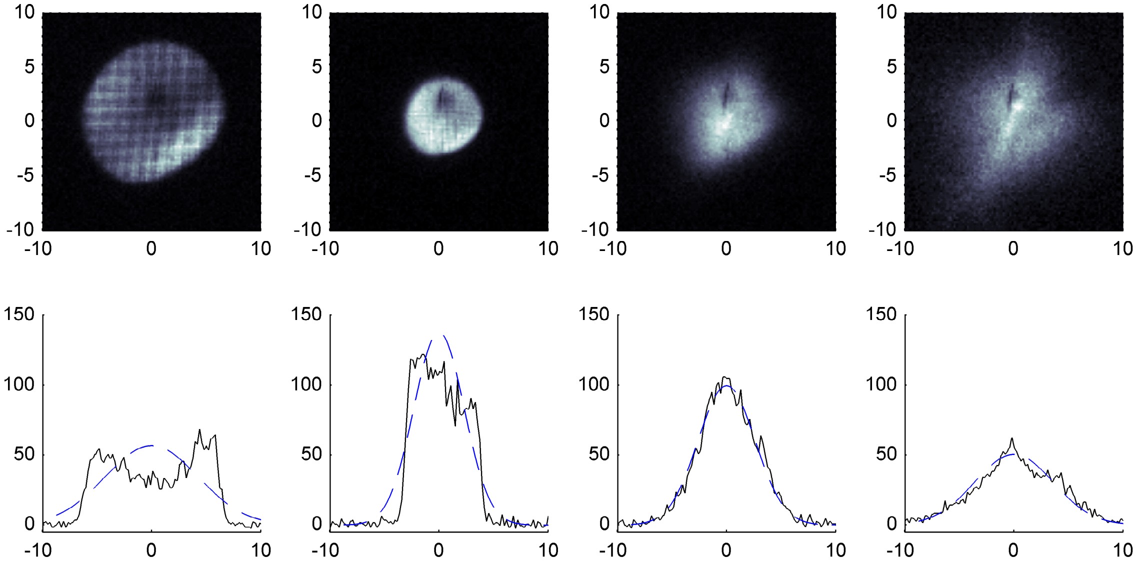

Figure 4.2: Ion projection images. (Top row) Example projection images at 0, 20, 60 and 100 μs after ionization. Axes are in mm, giving the size of the image at the MCP. (Bottom row) Image intensity along a slice through the center of the images; solid black line is the image intensity and dashed blue line is a Gaussian fit.

this magnification factor due to imperfect modeling of the electrodes. The lensing is fairly sensitive to the shape of the vacuum chamber, which is hard to precisely model. The chamber has a cylindrical base but there are various extensions (for optical access) that break the cylindrical symmetry and the distance between the grids and chamber walls has not been precisely measured. The grids are also connected by four stainless steel posts (separated by insulating spacers), and the effect of the square geometry of the posts is evident in the later time images, when the plasma is larger (Fig. 4.2).

Notice in Fig. 4.2 that we also see a grid structure in the images at earliest time. This is possibly due to secondary ion emission from the heavy Xe* ions striking the stainless steel mesh. If we reduce the magnitude of the voltage pulse, giving less energetic ions, the grid pattern disappears, but the lensing is also changed. There are also features that appear as dark or bright spots at the same location in all images that are likely due to localized degradation of the MCP sensitivity with age.

Finally, there is a background signal of ions striking the MCP that must be eliminated in late-time images. Around 70 μs after ionization, the plasma is large enough that ions start crossing the bottom grid and, with ion selecting voltages, get accelerated to the detector. This detection rate is exactly the ion signal, Fig. 1.6. When we take projection images after about 100 μs, the ions that struck the detector prior to the voltage pulse create a background signal. We wait to open the camera shutter until after the time of the voltage pulse, so we only collect light after the projection. But, there is some residual illumination from the earlier arriving ions due to the finite decay time of the phosphor fluorescence. For a clean pulse of ions on the detector, we delay the camera shutter and measure the 1/e lifetime of the phosphor fluorescence to be 50 μs, long enough to create a significant background. To eliminate this, we take a second image where the ions are pushed away from the detector at the projection time, giving us just the signal of the early arriving ions, and we subtract this from the projected image.

Despite these complications, Fig. 4.2 shows that we can observe the expansion of the plasma in the ion images and we have used this technique primarily for measurements of expansion in magnetic fields.

4.2 Uniform Magnetic Fields

For experiments in magnetic fields, we can not turn on a field in a time-scale shorter than the time it takes ions to accelerate in the plasma (1-10 μs). Thus we turn on the field before creating the plasma, but after turning off the MOT. Figure 1.2 shows the location of the magnetic field generating coils in our setup. The longitudinal coils generate a uniform field of 7.0 G/A. In previous work, the longitudinal coils were used to measure expansion in magnetic fields up to 70 G [23].

In the absence of a magnetic field, we simply use the MOT beams as the first transition of the two-photon ionization. In a magnetic field, the $6s[3/2]_2$ and $6p[5/2]_3$ states split into 5 and 7 magnetic sublevels. The transitions are shifted out of resonance with the MOT beams, so the ionization fractions we can achieve decrease for increasing field strength. We instead use the probe beam in Fig. 1.2, which is propagating perpendicular to the field axis, is π-polarized and is tuned to the field-independent $m = 0 \rightarrow m = 0$ transition. This maintains an ionization fraction of at least 20% of the zero-field value. We can achieve slightly better ionization fractions by sending three frequencies, detuned -5, 0 and 5 MHz from the $m = 0 \rightarrow m = 0$ transition, in the probe beam. A short pulse of these three frequencies is applied while the magnetic field is being turned on to optically pump atoms into the $m = 0$ ground state [30].

The previous work using the longitudinal coils was only able to measure the plasma expansion transverse to the magnetic field. We would also like to determine how the expansion along the magnetic field is altered, if at all. To do this, we added the transverse coils in Fig. 1.2. These coils are also perpendicular to the probe beam, so we can use the same ionization scheme with a simple rotation of the polarization axis.

The transverse coils are farther away and generate a field of only 0.45 G/A. To achieve large fields, we use a capacitor discharge circuit to turn on the magnetic field in 1.5 ms. The capacitance is chosen to make the discharge circuit slightly overdamped, with the peak current at 1.6 ms. During the 200 μs plasma lifetime, the magnitude of the current changes by less than 2%. We can create transverse fields up to 100 G.

The advantage of the transverse coils is that both the fast expansion along the field lines and the slow expansion transverse to the field can be seen in the projection images. A series of images taken in a transverse field at varying times during expansion is shown in Fig. 4.3, where the elongation of the plasma along the field lines is clear.

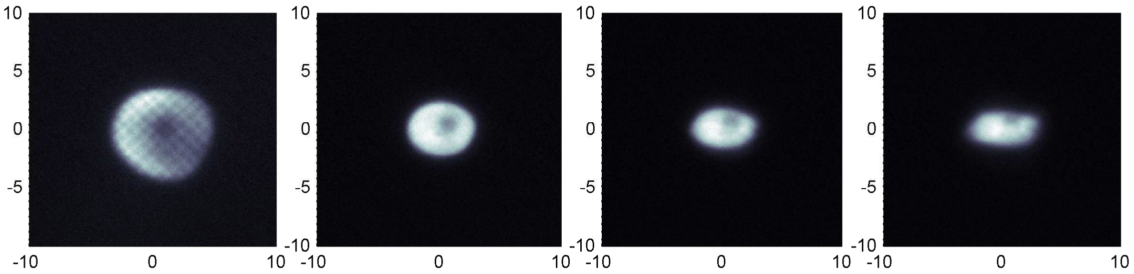

Figure 4.3: Ion projection images in a transverse magnetic field. Images taken at 0, 20, 40 and 60 μs after ionization in a transverse magnetic field of 18 G. Axes are in mm, giving the size of the image at the MCP.

We take a similar series of images for varied strengths of magnetic field and fit a 2D Gaussian to each of the images to extract a size. The results are shown in Fig. 4.4. The fits are applied to the images after subtracting the background signal, but we have not corrected for the Coulomb explosion or ion optic lensing.

Transverse to the field, we see that the late-time size of the images is significantly reduced for larger field. The expansion velocity transverse to the field decreases as $B^{-1/2}$ as described in [23]. For the data in Fig. 4.4, expansion along the field lines is slightly faster than in zero field, but mostly independent of the field strength. However, the Gaussian fits to images taken with different electrode voltages do not consistently show this trend. The fitted sizes are sometimes closer to the zero-field size and sometimes slightly less; the dark feature near the center of the images often makes the 2D Gaussian fits somewhat questionable. The previous study of UCP expansion assumed an unchanged expansion along the field lines [23], and we do not see significant deviation from this expectation. Improvements to the ion imaging system will be needed to generate more accurate results.

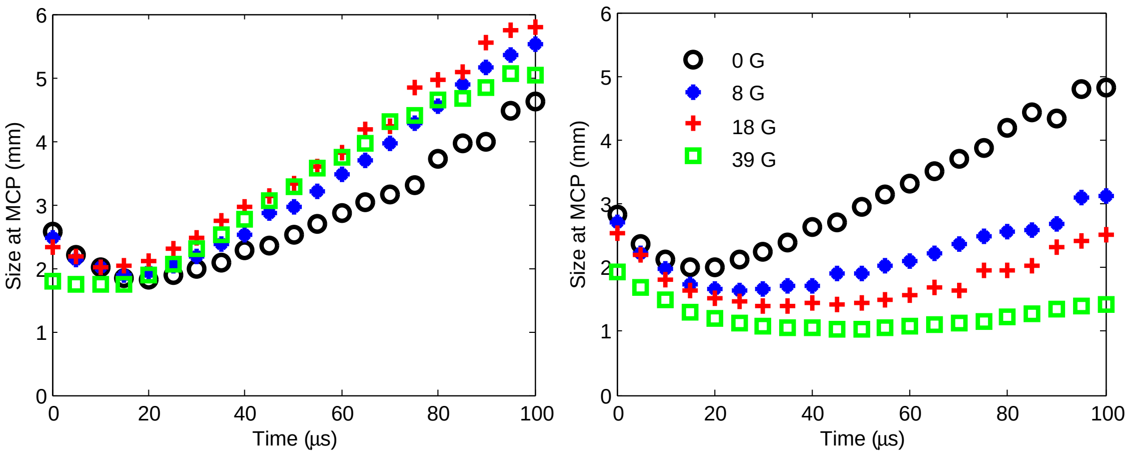

Figure 4.4: Plasma expansion in a magnetic field. Expansion along (left) and transverse to (right) the magnetic field direction. Sizes are rms widths of 2D Gaussian fits to the ion projection images. At early time, the size at the detector is large due to Coulomb explosion during time-of-flight. The difference in initial size reflects a smaller number of atoms ionized in larger field. All data was taken with $E_e/k_b = 100$ K.

4.3 Ion Current Signal

4.3.1 Ion Signal as a Measure of Expansion

The ion current signal, introduced in Sec. 1.4, also provides a measure of plasma expansion. First, consider the expansion without a magnetic field. We collect the current of ions on the MCP as they expand past the bottom grid. Ion current signals for different initial electron energies and no applied electric field (there are still stray fields) are shown in Fig. 4.5. We have fit each signal to the theory for a self-similar Gaussian expansion, extracting the asymptotic expansion velocity, the values given in Fig. 4.5(d). At initial energies $E_e > 60$ K the self-similar expansion model is an excellent fit to the data signals. For lower E_e, the TBR heating causes

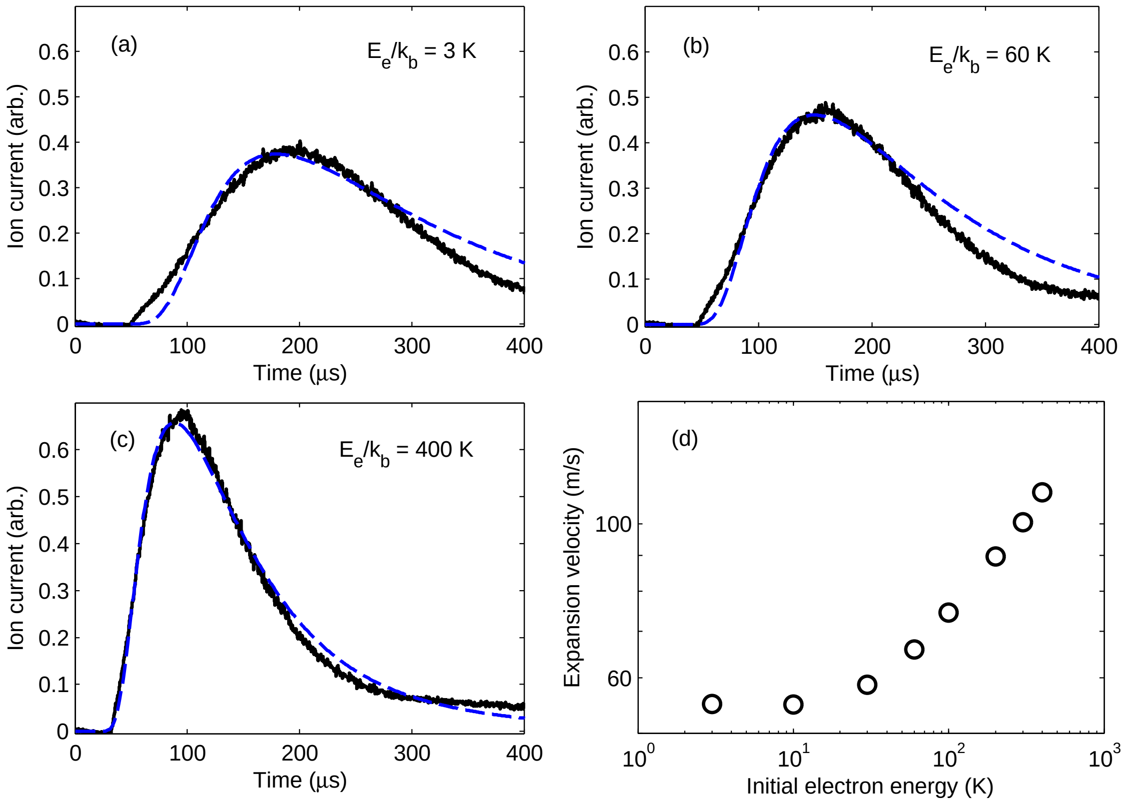

Figure 4.5: Ion current signals for varied initial temperature. (a)-(c) Measured ion current signals (black line) compared with calculation (dashed blue line) with $E_e/k_b = 3$, 60 and 400 K. (d) Expansion velocities from fits to the ion signals.

the expansion velocity to be faster than expected and the curves are not fit as well by the ideal model. The importance of TBR in altering UCP expansion has been well documented [22, 23, 34, 37].

For E_e/k_b between 100 K and 400 K, we can fit a power law function $v_0 \propto (E_e)^x$ and find an exponent of only $x = 0.35$, less than the 0.5 expected from the analytic solution (Eq. 1.9). It is unclear what causes this difference, but previous data from our lab using the ion projection imaging [23] also found a low value of $x = 0.44$.

The calculation does not account for the influence of applied or stray electric fields. An applied positive or negative electric field does cause the ion current to arrive slightly earlier or later, but the effect is much less dramatic than the influence seen in the electron signal. A field of 30 mV/cm in either direction does not change the fitted expansion velocities by more than ±10%, and we expect any stray fields to be less than this.

The ion signal has proven very useful as a routine diagnostic of plasma expansion; it is a single-shot measurement that requires no perturbations to the plasma.

4.3.2 Ion Density Spike

We can also monitor the ion current during experiments in uniform magnetic fields where expansion is not as well understood. Figure 4.6 shows the ion signal for a variety of strengths of transverse magnetic field. We know from our ion image measurements that the plasma expansion is slowed transverse to the field, so we would expect the MCP signal to start at later times for greater magnetic field strengths. Fig. 4.6 shows that the ion current does stretch to later times when the field is increased, but the time at which the first ions start crossing the grid is surprisingly constant and a step feature is visible at higher fields.

We speculate that the step feature at the beginning of the ion signals is related to the initial charge imbalance in the plasma. The prompt loss of electrons after ionization leaves a small net positive charge in the plasma. Previous simulations of the plasma expansion (without a magnetic field) predicted that the excess charge would cause a buildup of ions in an outwardly expanding shell at the leading edge

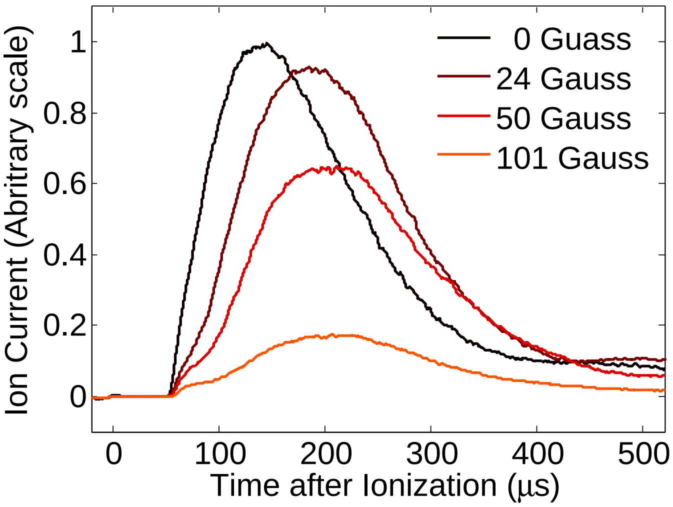

Figure 4.6: Ion current signals in a transverse magnetic field. We have not calibrated the gain on our MCP, so the actual number of ions detected is not known, but the same MCP gain was used for all data, so the relative size is accurate. Fewer ions are detected in larger fields both because fewer atoms are ionized, and because fewer ions make it past the bottom grid during expansion.

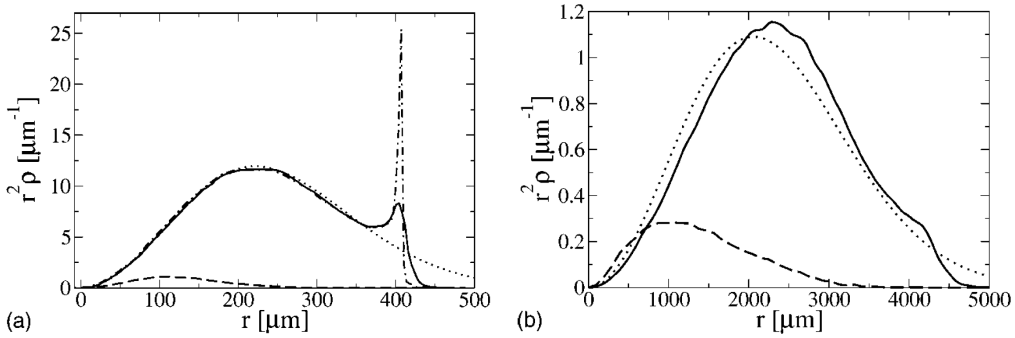

Figure 4.7: Simulated ion density. Spatial densities ρ_i (solid) and ρ_a (dashed) of the ions and atoms, respectively, at t=3 μs (a) and t=31.3 μs (b), compared to the Gaussian profile (dotted). Additionally, ρ_i obtained from the simulation using the zero-temperature fluid model only is shown as the dot-dashed line in (a), which indicates the extent to which the density spike is reduced by finite temperature. Reprinted from [35].

of the plasma. This was first predicted by Robicheaux and Hanson [34] using a zero-temperature fluid model for the ions and calculating the fluid motion in the self-consistent field of the electrons. Pohl et al [35] included finite temperature by doing a full molecular dynamics simulation of the ions in the mean-field of the electron fluid. Example results from the latter simulation are shown in Fig. 4.7. For typical UCP parameters, this density spike propagates outward at about the same speed as the plasma expansion and thus stays near the edge of the plasma. This density spike has not yet been observed in experiments.

UCP expansion in a magnetic field has not been simulated in the same way, but we expect a similar development of a density spike near the edge of the expanding plasma. But in a magnetic field, the plasma expansion is slowed transverse to the field lines, allowing for the possibility that the shell of ions could expand a significant distance ahead of the slowed plasma, causing the early-arriving feature in the ion current. This may explain why the arrival time of the first ions is not changed with stronger transverse field. Note that the magnetic fields we use are too small to alter the trajectory of free ions (the cyclotron period for a Xe* ion in a 10 G field is 9 ms, much longer than the plasma lifetime).

Even in the ion signals without a magnetic field, we note that the initial flux of ions has a sharp edge to it, rather than the smooth increase expected for a perfectly Gaussian density. The sharpness of the initial ion flux may be an indication of the ion spike crossing the grid just before the Gaussian cloud does.

As a simple way to explain the signals, we consider a model that separates the excess ions (due to the initial charge imbalance) from the rest of the neutral plasma. We can then think of the free ions as undergoing a Coulomb explosion, just like that described in our analysis of ion projection images. The speed at which the free ions expand depends on the absolute number of ions and the initial size.

This model is qualitatively consistent with the data. Figure 4.8 shows how the start of the ion signal in a transverse field changes with variations in initial electron temperature and in ion number. We see that at greater temperatures the step feature arrives earlier; this is because at greater temperatures more electrons escape upon ionization leaving behind a greater excess of ions [4]. For lower density plasmas, the scaled signals show that the step feature makes up a larger portion of the plasma signal, which is consistent with the fact that the initial charge imbalance (the fraction of lost electrons) is greater in smaller plasmas. We also see that the lower density plasmas produce a signal with a slightly later start time. This suggests that the absolute number of free ions is larger for a larger plasma, which is likely

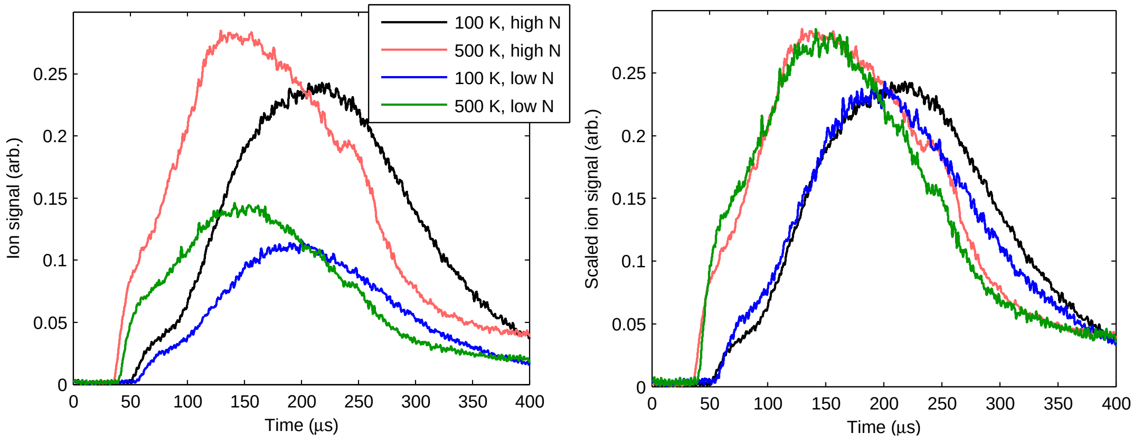

Figure 4.8: Scaled ion current signals in a transverse magnetic field. (Left) Recorded ion signals in a 50 G transverse field for different initial electron energy (E_e/k_b) and different number of atoms ionized. (Right) The same signals scaled to have the same integrated area.

still true even though the fraction of free ions is smaller.

We attempt to quantify this simple model as follows. Let f be the fraction of free ions, set equal to the initial charge imbalance. The time evolution of the density of the neutral plasma is assumed to follow a self-similar expansion of an elliptic Gaussian:

$$n_i(t) = \frac{N_i(1-f)}{(2\pi)^{3/2}\sigma_r^2(t)\sigma_z(t)} e^{-r^2/(2\sigma_r^2(t))} e^{-z^2/(2\sigma_z^2(t))} \tag{4.1}$$

where $\sigma_z(t) = \sqrt{\sigma_z(0)^2 + v_z^2 t^2}$, $\sigma_r(t) = \sqrt{\sigma_r(0)^2 + v_r^2 t^2}$, and v_z and v_r are the expansion velocities along and transverse to the field. We take v_z to be equal to the measured expansion velocity without a magnetic field. The flux of ions from the neutral plasma crossing the grid is calculated from Eq. 1.14 (Note that the cylindrical coordinate systems used for the expanding plasma and the grid system are not the same).

Separately, the free ions $N_{free} = fN_i$ are allowed to Coulomb explode starting from their initial density profile. We split the initial density into a series of concentric shells of equal charge (as described for the ion imaging), calculate the acceleration of the shells and iterate their positions. The flux of ions from the free ion explosion is calculated as each shell crosses the grid. The flux from the two separate parts are added together to produce the simulated ion current signal.

We tried two different initial density distributions for the free ion Coulomb explosion. In the first, excess ions are arranged in a spherical Gaussian with the same characteristic length as the rest of the plasma. In this case, the ion density develops a spike in the density profile, exactly as in Fig. 4.1(a). The speed at which the spike develops depends on the absolute number of free ions, N_{free}.

For the second model, we used an initial ion density with a uniform spatial distribution. Under Coulomb explosion, an initially uniform distribution stays uniform, which simplifies the calculation. The choice is also reasonable, since the plasma electrons very quickly equilibrate in the first few μs after creation to give a constant total plasma density given by Eq. 2.7 (from the analytic solution to a UCP without external fields). The excess ions, therefore, were arranged in a sphere with the constant density determined by Eq. 2.7 and whose radius was selected to give the proper number of excess ions. The choice is an approximation of the total plasma density after initial equilibration, like that calculated from the self-consistent solution of Poisson's equation in Fig. 2.7(b).

This second initial density choice produces more accurate fits of the data, some of which are shown in Fig. 4.9. The first density choice produces features in the ion

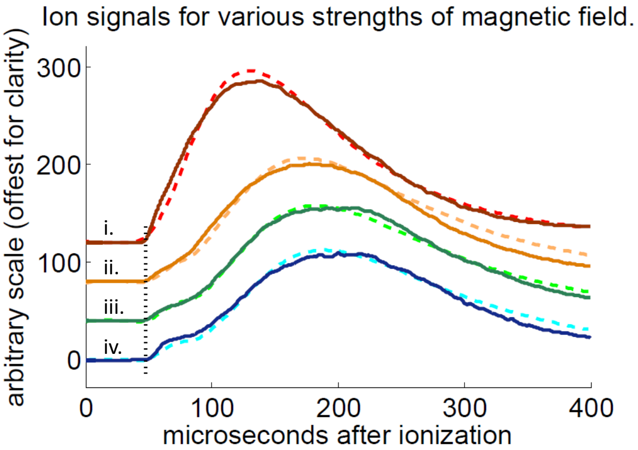

Figure 4.9: Ion current signals compared to density spike model. Ion signals (solid lines) for (i) 0, (ii) 24 G, (iii) 50 G and (iv) 101 G and the corresponding fits from the Gaussian plasma plus Coulomb explosion model (dashed lines). The model used $v_z = 70$ m/s and found values of (i) $N_{free} = 7 \times 10^4$, $v_r = 70$ m/s; (ii) $N_{free} = 3.5 \times 10^4$, $v_r = 59$ m/s; (iii) $N_{free} = 3.5 \times 10^4$, $v_r = 56$ m/s; (iv) $N_{free} = 3.5 \times 10^4$, $v_r = 53$ m/s.

flux that are sharper than our observations, but this may just be a reflection of the zero-temperature Coulomb explosion calculation; even within the separated model, finite temperature ions would smooth the results.

Figure 4.9 shows that our model can produce good fits to the data. The fits give reasonable estimates for the number of free ions, but they give values for the transverse expansion velocity that are larger than the asymptotic velocities measured from the ion images. The discrepancy is likely due to the inadequacy of the self-similar expansion model for the plasma expanding across the magnetic field.

A problem with both the ion signal and ion image measurements of expansion is that we only measure expansion at late time. The ion signal gives no information before ions start crossing the grid, and the Coulomb explosion during time-of-flight disrupts the imaging measurements. One possibility is that the transverse expansion velocity is near the zero-field value immediately after creation but then decreases and levels off to a smaller value at late time. This type of expansion may be sufficient to explain all of the observations.

Regardless of the exact form of plasma expansion, we have shown our observations to be consistent with the presence of an ion density spike expanding ahead of the plasma as previously predicted.

4.4 Magnetic Trapping Geometries

We finally consider three-dimensional magnetic trapping geometries. Using the longitudinal coils and reversing the current direction in one of them we can apply a quadrupole, or cusp, magnetic field up to 100 G/cm. A cusp field has a minimum in the magnetic field magnitude at its center and provides a three-dimensional confining force for magnetized electrons due to the mirror force. We present here preliminary data on the plasma expansion in a cusp field. The combination of the ion signal and ion projection images allows us to monitor the ion expansion in all three dimensions and show a three-dimensional slowing of the expansion.

Fig. 4.10 shows a sequence of ion projection images taken in a cusp field of 35 G/cm. Changes in shape from $B = 0$ expansion will be hard to quantify due to the complications during time-of-flight, but we can use the images to track the general size of the plasma over time. Fig. 4.11 shows the size of the images from 2D

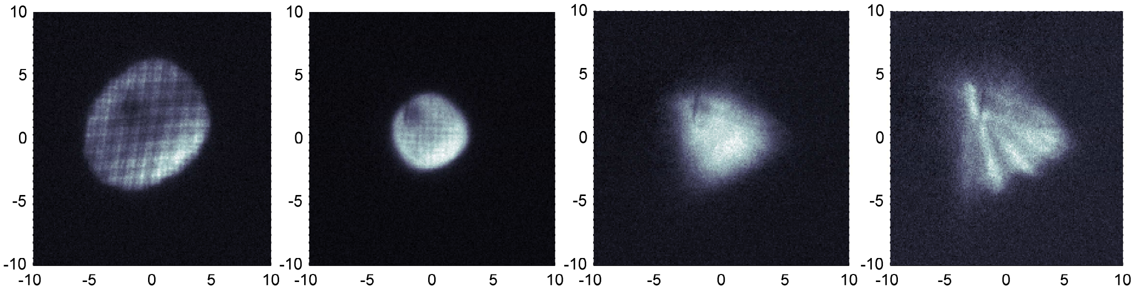

Figure 4.10: Ion projection images in a cusp field. Images taken (left to right) 0, 20, 60 and 100 μs after ionization of a plasma with $E_e/k_b = 100$ K. The cusp field has a 35 G/cm gradient at the center. Axes in mm.

Gaussian fits taken for varied strength of the cusp field, with the late time size clearly reduced for stronger fields. We also show measurements of the ion current signal, which compliments the projection images since it measures the expansion along the grid axis. For stronger cusp fields, the ion signal changes shape and clearly shows a reduced expansion rate. The combination of the measurements indicates a 3D reduction of plasma expansion.

The basic idea of 3D confinement is understood by considering single-particle trajectories. Simple magnetic trapping geometries, like the cusp field and magnetic bottle, make use of the mirror force which reflects charged particles traveling up a magnetic field gradient. Assuming the magnetic field changes slowly in space compared to the radius of the electron cyclotron motion, the magnetic moment of the electron is a constant (adiabatic invariant) of the motion. A particle traveling from a region of low to high magnetic field feels a force proportional to the magnetic moment and the field gradient

$$F_z = -\mu \frac{dB_z}{dz} = -\frac{m v_\perp^2}{2B} \frac{dB_z}{dz} \tag{4.2}$$

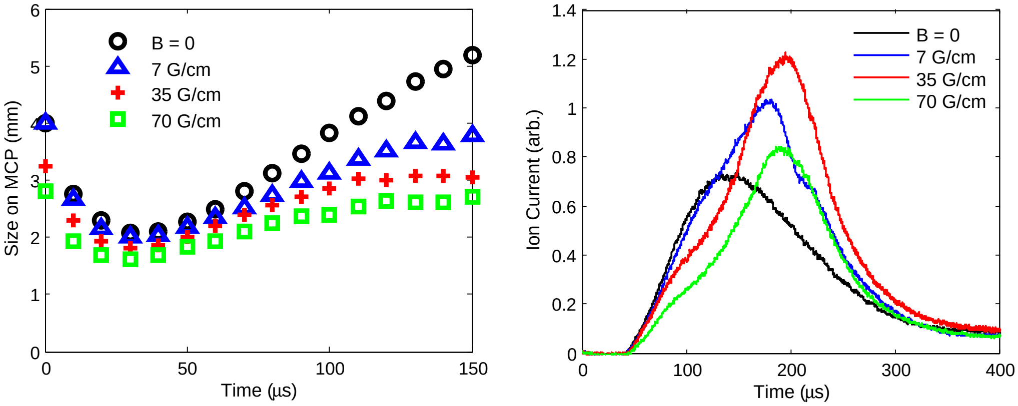

Figure 4.11: Plasma expansion in a cusp field. (Left) Size (rms width) of plasma calculated from a symmetric 2D Gaussian fit to ion images for varied strength cusp field. (Right) Ion current signals in the same cusp fields.

where μ is the magnetic moment and $v_\perp$ is the velocity component transverse to the magnetic field. The trapping is dependent on the direction of the velocity of the electrons; electrons traveling mostly along the field lines feel a smaller force and more easily escape the system. Efforts to confine hot plasmas for fusion reactions have largely abandoned the use of cusp and bottle fields due to these losses.

The low temperature of our plasma electrons means the effect of the mirror force is small. For realistic field gradients, the force is equivalent to that from an electric field of at most a few 10s of mV/cm, not much more than the size of stray electric fields in our vacuum chamber. The low temperature also comes with a high collision rate which diminishes the effectiveness of the trap, as electrons in stably trapped orbits are frequently knocked onto escape trajectories. While single particle trajectories in a cusp field can be easily calculated, understanding the diffusion of our neutral plasma in this field will be very challenging.

We have also considered a magnetic bottle geometry. A magnetic bottle consists of a pair of identical coils carrying the same current placed symmetrically on either side of the plasma with a separation greater than the coil radius, such that there is a magnetic field minimum at the center. Unfortunately the geometry of our vacuum chamber is not well suited for applying a strong magnetic bottle. We have investigated other vacuum chamber geometries that would allow us to put coils closer to the plasma in order to have a significant mirror ratio across the plasma, where the mirror ratio is the ratio of the maximum magnetic field seen by the plasma to the minimum magnetic field at the center of the trap.

There are two main challenges in any design. First, the need for optical access limits the possible coil locations. The geometry of laser beams used to cool and trap atoms in the MOT (Fig. 1.2) is the main limitation. Reducing the beam sizes below the current 2.5 cm diameter reduces the capture volume and the number of atoms trapped. The second issue is the plasma expansion. Ideally, we would like a large mirror ratio over the diameter of the plasma, but the plasma changes in size by orders of magnitude during expansion. Placing the coils closer gives a better mirror ratio at plasma creation, but less time to study expansion before the plasma hits the magnets. Placing them far enough away to allow for significant expansion ensures a small, perhaps negligible, mirror ratio during the initial ion acceleration.

The advantage of a bottle field over a cusp field is that the plasma is created in a region of non-zero field and we know from our experiments in uniform fields that the expansion can be significantly reduced in the transverse direction. But the small mirror ratio at early times suggests the expansion along the field lines may not be significantly reduced and there is little reason to expect slower expansion than that seen in our cusp field measurements.

Chapter 5

Summary and Outlook

In this thesis, we have presented recent progress in experiments on ultracold neutral plasmas. This is the first analysis that considers the importance of the global charge imbalance and its effect on measurements made during plasma expansion.

We have described the growing number of diagnostic tools that enable us to probe both electron and ion dynamics in UCPs. We presented for the first time a complete understanding of the electron emission from UCPs. Our new understanding of the ion current signal, combined with ion projection imaging, proves that we can extract three-dimensional information about the ion density even in the absence of optical ion imaging capability. Our development of electronic detection of collective modes represents a new class of diagnostic that gives us access to plasma properties not available through charged particle or optical measurements.

In Chapter 2, we developed an improved understanding of the electron spatial distribution and the connection with the electron loss rate. Expanding ultracold neutral plasmas are systems in quasi-equilibrium, sharing this aspect with a wide variety of physical systems from atomic to galactic clusters. We presented data of electron evaporation in excellent agreement with a zero-temperature electron model, where the electrons arrange themselves in an asymmetric density distribution to exactly cancel the ion plus external electric fields. This result does not directly address the question of the form of the electron energy distribution function, but could serve as a foundation in further experiments. Our ability to directly detect the emitted particles as well as perturb the potential in a time dependent manner suggests that UCPs are a good candidate system to address fundamental questions about systems in quasi-equilibrium.

In Chapter 3, we used electronic mode detection to confirm the importance of the electron spatial distribution and electron loss on plasma oscillations. The electronic mode diagnostic has proved to be more accurate and more versatile than the previous method. It is also worth noting that we observe plasma resonances at much later times than are normally studied in UCPs. At 90 μs, the plasma density has dropped to 2×10^5 cm^{-3}, but we can still observe clear collective behavior, which is a testament to the extremely low electron temperature, expected to be less than 1 K at that time. Our new mode diagnostic also opens up the study of UCP collective modes to a rich spectrum of modes involving magnetized electrons that we have only begun to explore.

Improved electron temperature measurements are also possible. Existing methods for measuring the electron temperature have succeeded in proving that the electrons are heated to large temperatures even when the initial temperature is low. But these methods could only measure the temperature at later times after the majority of the heating had taken place. With our new rf probe, we can observe a non-zero plasma oscillation signal at times immediately after plasma creation. A better understanding of the rf signals will allow us to probe electron properties during initial plasma equilibration, which would be a significant advance.

In Chapter 4, we showed improved measurements on plasma expansion in uniform magnetic fields and the first attempt at magnetic confinement. We measured the ion current from a plasma expanding across a magnetic field, and find features that indicate a separation of the ion density due to the initial charge imbalance established during plasma creation. But there are still many open questions about the exact form of the ion density during expansion in a magnetic field. We have also not yet considered the importance of stray electric fields and electron loss in these experiments.

Another long-standing goal of UCP physics is to find ways to increase the correlations of either the ions or the electrons. There is no clear path to achieve strongly coupled electrons, and some theoretical models suggest that TBR will prevent strong coupling under any circumstances [20, 59]. But many proposals exist to create more strongly coupled ions, including laser-cooling of the ions [108, 109] and the loading of the atomic gas into an optical lattice prior to ionization [110]. The strong interactions between Rydberg atoms might also be used to establish initial correlations. Excitation to the Rydberg state with a narrow-linewidth laser could take advantage of the Rydberg blockade mechanism to excite a Rydberg gas with a more uniform spatial distribution. Some of these proposals could be implemented in our system, but the challenge will be in detecting the strong coupling without the ability to optically probe the ions.

As the field of UCP research has grown, there have been increasing connections to traditional areas of plasma physics, particularly laser-irradiated clusters and one-component plasmas. The high level of control and flexibility of ultracold neutral plasmas presents many opportunities for future work that are likely to produce exciting and unexpected results.

Appendix A

Cold Electron Algorithm

This appendix summarizes the numerical algorithm used to calculate the boundary of the zero-temperature electron distribution.

The algorithm defines a boundary for the electron cloud as an array of z, s points (where s is the cylindrical radial coordinate). The boundary is initially defined as being at the edge of the ion density. The total charge density is equal to the ion density for points outside the electron boundary and equal to zero for points inside the boundary. For each point on the boundary, we calculate the local electric field from the combination of the total charge density and the external field. We then move the boundary point by an amount proportional to the field. The total charge density is recalculated and the process is repeated over many iterations.

Even though the boundary is defined in cylindrical coordinates, the electric field is calculated in spherical coordinates (r, θ) centered at the center of the ion cloud. The boundary could have been defined in spherical coordinates but there was a problem with that at high fields. The algorithm defines the boundary as a single value of r for evenly spaced points in θ (or now s as a function of z). But when the boundary is small and offset such that the origin is outside the boundary, then it can not be written as a single-valued function $r(\theta)$. Cylindrical coordinates work better.

The idea is that the algorithm slows down and stops as the local electric field approaches zero at all boundary points. However, the condition $E_r = E_\theta = 0$ at each boundary point does not define a unique solution. In fact, a solution will exist for every value of electron fraction N_e/N_i up to a certain maximum. We seek only the solution that gives this maximum value.

We calculate the potential along the z-axis on each step and wait for it to flatten out. The exit condition is when the boundary overshoots and a dip is visible in the potential. This gets within < 0.05 of the right answer for N_e/N_i. We found that we obtained better precision by making some ad hoc additions after letting this main algorithm finish; the low density outer regions are the most problematic.

The calculation of the electric field at each boundary point is done efficiently as follows [111]. We expand the charge density ρ and the potential ψ generated by the plasma in terms of N Legendre polynomials. We can then express the electric field in terms of a sum over N and an integral over the radial coordinate r.

The charge density is expressed in a spherical coordinate system centered at the center of the ion cloud. The electrostatic potential generated by the plasma obeys Poisson's equation with azimuthal symmetry

$$\frac{1}{r^2}\frac{d}{dr}\left(r^2\frac{d\psi}{dr}\right)+\frac{1}{r^2 sin\theta}\frac{d}{d\theta}\left(sin\theta\frac{d\psi}{d\theta}\right)=-4\pi\rho \tag{A.1}$$

Expand ψ and ρ in the first $N+1$ Legendre polynomials

$$\rho=\sum_{l=0}^{l=N}\rho_l\left(r\right)P_l\left(cos\theta\right) \tag{A.2}$$

$$\psi=\sum_{l=0}^{l=N}\psi_l\left(r\right)P_l\left(cos\theta\right) \tag{A.3}$$

where

$$\rho_l\left(r\right) = \frac{2l+1}{2}\int_0^{\pi}\rho\left(r,\theta\right)P_l\left(cos\theta\right)sin\theta d\theta \tag{A.4}$$

and we have used the identity

$$\int_0^{\pi}\rho P_l\left(cos\theta\right)sin\theta d\theta = \sum_{m=0}^{m=N}\rho_m\left(r\right)\int_{-1}^{1}P_m\left(x\right)P_l\left(x\right)dx = \rho_l\left(r\right)\frac{2}{2l+1} \tag{A.5}$$

The Poisson equation can now be rewritten

$$\frac{1}{r^2}\frac{d}{dr}\left(r^2\frac{d\psi_l}{dr}\right) - l\left(l+1\right)\frac{\psi_l}{r^2} = -4\pi\rho_l \tag{A.6}$$

Using a Green's function method, we can solve for the ψ_l

$$\psi_l = \frac{4\pi}{2l+1}\left(\int_0^r\rho_l(x)\left(\frac{x}{r}\right)^{l+1}xdx + \int_r^{\infty}\rho_l(x)\left(\frac{r}{x}\right)^{l}xdx\right) \tag{A.7}$$

and calculate the electric field to be

$$E_r = \frac{d\psi}{dr} = -\sum_{l=0}^{l=N}\frac{4\pi P_l\left(cos\theta\right)}{r\left(2l+1\right)}\left(l\int_r^{\infty}\rho_l(x)\left(\frac{r}{x}\right)^{l}xdx - \left(l+1\right)\int_0^r\rho_l(x)\left(\frac{x}{r}\right)^{l+1}xdx\right) \tag{A.8}$$

$$E_\theta = -\frac{1}{r}\frac{d\psi}{d\theta} = -\sum_{l=0}^{l=N}\frac{cos\theta P_l\left(cos\theta\right) - P_{l-1}\left(cos\theta\right)}{sin\theta}\frac{1}{r}\psi_l \tag{A.9}$$

In our algorithm, using $N = 30$ was sufficient.

Bibliography

[1] T. Killian, T. Pattard, T. Pohl, and J. Rost, Physics Reports **449**, 77 (2007).

[2] T. C. Killian, Science **316**, 705 (2007).

[3] T. C. Killian and S. L. Rolston, Physics Today **63**, 46 (2010).

[4] T. C. Killian, S. Kulin, S. D. Bergeson, L. A. Orozco, C. Orzel, and S. L. Rolston, Phys. Rev. Lett. **83**, 4776 (1999).

[5] M. P. Robinson, B. L. Tolra, M. W. Noel, T. F. Gallagher, and P. Pillet, Phys. Rev. Lett. **85**, 4466 (2000).

[6] A. Walz-Flannigan, J. R. Guest, J. Choi, and G. Raithel, Phys. Rev. A **69**, 063405 (2004).

[7] C. E. Simien, Y. C. Chen, P. Gupta, S. Laha, Y. N. Martinez, P. G. Mickelson, S. B. Nagel, and T. C. Killian, Phys. Rev. Lett. **92**, 143001 (2004).

[8] E. A. Cummings, J. E. Daily, D. S. Durfee, and S. D. Bergeson, Phys. Rev. Lett. **95**, 235001 (2005).

[9] J. P. Morrison, C. J. Rennick, J. S. Keller, and E. R. Grant, Phys. Rev. Lett. **101**, 205005 (2008).

[10] S. G. Kuzmin and T. M. O'Neil, Phys. Rev. Lett. **88**, 065003 (2002).

[11] S. G. Kuzmin and T. M. O'Neil, Phys. Plasmas **9**, 3743 (2002).

[12] S. Mazevet, L. A. Collins, and J. D. Kress, Phys. Rev. Lett. **88**, 055001 (2002).

[13] Y. C. Chen, C. E. Simien, S. Laha, P. Gupta, Y. N. Martinez, P. G. Mickelson, S. B. Nagel, and T. C. Killian, Phys. Rev. Lett. **93**, 265003 (2004).

[14] S. D. Bergeson, A. Denning, M. Lyon, and F. Robicheaux, Phys. Rev. A **83**, 023409 (2011).

[15] M. Lyon and S. D. Bergeson, J. Phys. B **44**, 184014 (2011).

[16] J. Castro, P. McQuillen, and T. C. Killian, Phys. Rev. Lett. **105**, 065004 (2010).

[17] P. McQuillen, J. Castro, and T. C. Killian, J. Phys. B **44**, 184013 (2011).

[18] P. Mansbach and J. Keck, Phys. Rev. **181**, 275 (1969).

[19] T. Pohl, D. Vrinceanu, and H. R. Sadeghpour, Phys. Rev. Lett. **100**, 223201 (2008).

[20] G. Bannasch and T. Pohl, Phys. Rev. A **84**, 052710 (2011).

[21] R. S. Fletcher, X. L. Zhang, and S. L. Rolston, Phys. Rev. Lett. **99**, 145001 (2007).

[22] S. Kulin, T. C. Killian, S. D. Bergeson, and S. L. Rolston, Phys. Rev. Lett. **85**, 318 (2000).

[23] X. L. Zhang, R. S. Fletcher, S. L. Rolston, P. N. Guzdar, and M. Swisdak, Phys. Rev. Lett. **100**, 235002 (2008).

[24] J. L. Roberts, C. D. Fertig, M. J. Lim, and S. L. Rolston, Phys. Rev. Lett. **92**, 253003 (2004).

[25] T. C. Killian, M. J. Lim, S. Kulin, R. Dumke, S. D. Bergeson, and S. L. Rolston, Phys. Rev. Lett. **86**, 3759 (2001).

[26] X. L. Zhang, R. S. Fletcher, and S. L. Rolston, Phys. Rev. Lett. **101**, 195002 (2008).

[27] M. S. Walhout, *Studies of Laser-Cooled and Magneto-Optically Trapped Xenon.*, Ph.D. thesis, University of Maryland, College Park. (1994).

[28] C. R. Orzel, *Ultracold ionizing collisions in metastable xenon*, Ph.D. thesis, University of Maryland, College Park (1999).

[29] R. S. Fletcher, *Three-body recombination and Rydberg atoms in ultracold plasmas*, Ph.D. thesis, University of Maryland, College Park (2008).

[30] X. Zhang, *Ultracold plasma dynamics in a magnetic field*, Ph.D. thesis, University of Maryland, College Park (2009).

[31] M. Walhout, A. Witte, and S. L. Rolston, Phys. Rev. Lett. **72**, 2843 (1994).

[32] H. J. Metcalf and P. van der Straten, *Laser Cooling and Trapping* (Springer-Verlag, New York, 1999).

[33] F. Robicheaux and J. D. Hanson, Phys. Rev. Lett. **88**, 055002 (2002).

[34] F. Robicheaux and J. D. Hanson, Phys. Plasmas **10**, 2217 (2003).

[35] T. Pohl, T. Pattard, and J. M. Rost, Phys. Rev. A **70**, 033416 (2004).

[36] S. Laha, P. Gupta, C. E. Simien, H. Gao, J. Castro, T. Pohl, and T. C. Killian, Phys. Rev. Lett. **99**, 155001 (2007).

[37] P. Gupta, S. Laha, C. E. Simien, H. Gao, J. Castro, T. C. Killian, and T. Pohl, Phys. Rev. Lett. **99**, 075005 (2007).

[38] L. Spitzer, *Physics of Fully Ionized Gases* (Wiley, New York, 1962).

[39] R. S. Fletcher, X. L. Zhang, and S. L. Rolston, Phys. Rev. Lett. **96**, 105003 (2006).

[40] J.-H. Choi, B. Knuffman, X. H. Zhang, A. P. Povilus, and G. Raithel, Phys. Rev. Lett. **100**, 175002 (2008).

[41] X. L. Zhang, R. S. Fletcher, and S. L. Rolston, AIP Conference Proceedings **1114**, 11 (2009).

[42] J. Castro, P. McQuillen, H. Gao, and T. C. Killian, Journal of Physics: Conference Series **194**, 012065 (2009).

[43] J. Castro, G. Bannasch, P. McQuillen, T. Pohl, and T. C. Killian, ArXiv e-prints (2011), arXiv:1112.3241 [physics.atom-ph] .

[44] H. Park, R. Ali, and T. F. Gallagher, Phys. Rev. A **82**, 023421 (2010).

[45] T. Pohl, T. Pattard, and J. M. Rost, Phys. Rev. A **68**, 010703 (2003).

[46] W. Li, M. W. Noel, M. P. Robinson, P. J. Tanner, T. F. Gallagher, D. Comparat, B. Laburthe Tolra, N. Vanhaecke, T. Vogt, N. Zahzam, P. Pillet, and D. A. Tate, Phys. Rev. A **70**, 042713 (2004).

[47] W. Li, P. J. Tanner, and T. F. Gallagher, Phys. Rev. Lett. **94**, 173001 (2005).

[48] N. Vanhaecke, D. Comparat, D. A. Tate, and P. Pillet, Phys. Rev. A **71**, 013416 (2005).

[49] M. Viteau, A. Chotia, D. Comparat, D. A. Tate, T. F. Gallagher, and P. Pillet, Phys. Rev. A **78**, 040704 (2008).

[50] P. J. Tanner, J. Han, E. S. Shuman, and T. F. Gallagher, Phys. Rev. Lett. **100**, 043002 (2008).

[51] M. Saffman, T. G. Walker, and K. Mølmer, Rev. Mod. Phys. **82**, 2313 (2010).

[52] G. Pupillo, A. Micheli, M. Boninsegni, I. Lesanovsky, and P. Zoller, Phys. Rev. Lett. **104**, 223002 (2010).

[53] J. E. Johnson and S. L. Rolston, Phys. Rev. A **82**, 033412 (2010).

[54] J. Honer, H. Weimer, T. Pfau, and H. P. Büchler, Phys. Rev. Lett. **105**, 160404 (2010).

[55] J. P. Morrison, C. J. Rennick, and E. R. Grant, Phys. Rev. A **79**, 062706 (2009).

[56] C. J. Rennick, N. Saquet, J. P. Morrison, J. Ortega-Arroyo, P. Godin, L. Fu, M. Schulz-Weiling, and E. R. Grant, Journal of Physics: Conference Series **300**, 012005 (2011).

[57] N. Saquet, J. P. Morrison, M. Schulz-Weiling, H. Sadeghi, J. Yiu, C. J. Rennick, and E. R. Grant, J. Phys. B **44**, 184015 (2011).

[58] H. Sadeghi, M. Schulz-Weiling, J. P. Morrison, J. C. H. Yiu, N. Saquet, C. J. Rennick, and E. Grant, Phys. Chem. Chem. Phys. **13**, 18872 (2011).

[59] K. Niffenegger, K. A. Gilmore, and F. Robicheaux, J. Phys. B **44**, 145701 (2011).

[60] R. C. Davidson, *Physics of Nonneutral Plasmas* (Addison-Wesley, Redwood City, California, 1990).

[61] T. M. O'Neil, Physics Today **52**, 24 (1999).

[62] D. H. E. Dubin and T. M. O'Neil, Rev. Mod. Phys. **71**, 87 (1999).

[63] S. L. Gilbert, J. J. Bollinger, and D. J. Wineland, Phys. Rev. Lett. **60**, 2022 (1988).

[64] T. B. Mitchell, J. J. Bollinger, D. H. E. Dubin, X.-P. Huang, W. M. Itano, and R. H. Baughman, Science **282**, 1290 (1998).

[65] G. B. Andresen *et al.*, Nature **468**, 673 (2010).

[66] G. B. Andresen *et al.*, Nat. Phys. **7**, 558 (2011).

[67] B. J. Claessens, S. B. van der Geer, G. Taban, E. J. D. Vredenbregt, and O. J. Luiten, Phys. Rev. Lett. **95**, 164801 (2005).

[68] J. L. Hanssen, J. J. McClelland, E. A. Dakin, and M. Jacka, Phys. Rev. A **74**, 063416 (2006).

[69] M. P. Reijnders, P. A. van Kruisbergen, G. Taban, S. B. van der Geer, P. H. A. Mutsaers, E. J. D. Vredenbregt, and O. J. Luiten, Phys. Rev. Lett. **102**, 034802 (2009).

[70] M. P. Reijnders, N. Debernardi, S. B. van der Geer, P. H. A. Mutsaers, E. J. D. Vredenbregt, and O. J. Luiten, Phys. Rev. Lett. **105**, 034802 (2010).

[71] A. V. Steele, B. Knuffman, J. J. McClelland, and J. Orloff, J. Vac. Sci. Technol. B **28**, C6F1 (2010).

[72] A. J. McCulloch, D. V. Sheludko, S. D. Saliba, S. C. Bell, M. Junker, K. A. Nugent, and R. E. Scholten, Nat. Phys. **7**, 785 (2011).

[73] J.-M. Rost, European Review **17**, 249 (2009).

[74] T. Fennel, K.-H. Meiwes-Broer, J. Tiggesbäumker, P.-G. Reinhard, P. M. Dinh, and E. Suraud, Rev. Mod. Phys. **82**, 1793 (2010).

[75] T. D. Donnelly, T. Ditmire, K. Neuman, M. D. Perry, and R. W. Falcone, Phys. Rev. Lett. **76**, 2472 (1996).

[76] T. Ditmire, J. Zweiback, V. P. Yanovsky, T. E. Cowan, G. Hays, and K. B. Wharton, Nature **398**, 489 (1999).

[77] I. Alexeev, T. M. Antonsen, K. Y. Kim, and H. M. Milchberg, Phys. Rev. Lett. **90**, 103402 (2003).

[78] T. Pohl and T. Pattard, J. Phys. A **39**, 4571 (2006).

[79] D. Comparat, T. Vogt, N. Zahzam, M. Mudrich, and P. Pillet, Mon. Not. R. Astron. Soc. **361**, 1227 (2005).

[80] D. Vrinceanu, G. S. Balaraman, and L. A. Collins, J. Phys. A **41**, 425501 (2008).

[81] K. A. Twedt and S. L. Rolston, Phys. Plasmas **17**, 082101 (2010).

[82] B. Breizman and A. Arefiev, Plasma Physics Reports **29**, 593 (2003).

[83] B. Breizman, A. Arefiev, and M. Fomytskyi, Phys. Plasmas **12**, 056706 (2005).

[84] R. W. Michie, Mon. Not. R. Astron. Soc. **125**, 127 (1963).

[85] I. R. King, Astron. J. **71**, 64 (1966).

[86] O. J. Luiten, M. W. Reynolds, and J. T. M. Walraven, Phys. Rev. A **53**, 381 (1996).

[87] G. B. Andresen *et al.* (ALPHA Collaboration), Phys. Rev. Lett. **105**, 013003 (2010).

[88] M. Hobein, A. Solders, M. Suhonen, Y. Liu, and R. Schuch, Phys. Rev. Lett. **106**, 013002 (2011).

[89] S. D. Bergeson and R. L. Spencer, Phys. Rev. E **67**, 026414 (2003).

[90] A. Lyubonko, T. Pohl, and J.-M. Rost, ArXiv e-prints (2010), arXiv:1011.5937 [physics.plasm-ph] .

[91] K. A. Twedt and S. L. Rolston, ArXiv e-prints (2011), arXiv:1110.6909 [physics.plasm-ph] .

[92] D. J. Wineland and H. G. Dehmelt, J. Appl. Phys. **46**, 919 (1975).

[93] C. S. Weimer, J. J. Bollinger, F. L. Moore, and D. J. Wineland, Phys. Rev. A **49**, 3842 (1994).

[94] M. D. Tinkle, R. G. Greaves, C. M. Surko, R. L. Spencer, and G. W. Mason, Phys. Rev. Lett. **72**, 352 (1994).

[95] M. D. Tinkle, R. G. Greaves, and C. M. Surko, Phys. Plasmas **2**, 2880 (1995).

[96] M. Amoretti *et al.* (ATHENA Collaboration), Phys. Rev. Lett. **91**, 055001 (2003).

[97] M. Amoretti *et al.*, Phys. Plasmas **10**, 3056 (2003).

[98] N. Kuroda, H. A. Torii, K. Y. Franzen, Z. Wang, S. Yoneda, M. Inoue, M. Hori, B. Juhász, D. Horváth, H. Higaki, A. Mohri, J. Eades, K. Komaki, and Y. Yamazaki, Phys. Rev. Lett. **94**, 023401 (2005).

[99] A. Speck, G. Gabrielse, P. Larochelle, D. L. Sage, B. Levitt, W. Kolthammer, R. McConnell, J. Wrubel, D. Grzonka, W. Oelert, T. Sefzick, Z. Zhang, D. Comeau, M. George, E. Hessels, C. Storry, M. Weel, and J. Walz, Phys. Lett. B **650**, 119 (2007).

[100] L. Tonks, Phys. Rev. **37**, 1458 (1931).

[101] A. Dattner, Phys. Rev. Lett. **10**, 205 (1963).

[102] J. V. Parker, J. C. Nickel, and R. W. Gould, Phys. Fluids **7**, 1489 (1964).

[103] A. Lyubonko, T. Pohl, and J. M. Rost, Private communication.

[104] F. F. Chen, *Introduction to Plasma Physics and Controlled Fusion* (Springer, New York, 1984).

[105] F. Anderegg, N. Shiga, J. R. Danielson, D. H. E. Dubin, C. F. Driscoll, and R. W. Gould, Phys. Rev. Lett. **90**, 115001 (2003).

[106] N. Shiga, F. Anderegg, D. H. E. Dubin, C. F. Driscoll, and R. W. Gould, Phys. Plasmas **13**, 022109 (2006).

[107] D. Feldbaum, N. V. Morrow, S. K. Dutta, and G. Raithel, Phys. Rev. Lett. **89**, 173004 (2002).

[108] T. Pohl, T. Pattard, and J. M. Rost, Phys. Rev. Lett. **92**, 155003 (2004).

[109] T. Pohl, T. Pattard, and J. M. Rost, J. Phys. B **38**, S343 (2005).

[110] T. Pohl, T. Pattard, and J. M. Rost, J. Phys. B **37**, L183 (2004).

[111] A. Arefiev, Private communication.